CANCER

A window-of-opportunity trial reveals mechanisms of response and resistance to navtemadlin in patients with recurrent glioblastoma

Veronica Rendo[1,2,3,4,5]*†, Eudocia Q. Lee[1,3,6]*†, Connor Bossi[7], Nicholas Khuu[1,2,4], Michelle A. Rudek[8]‡, Sangita Pal[1,2,3,4], Narmen Azazmeh[1,2,3,4], Rumana Rashid[9,10], Jia-Ren Lin[11], Margaret Cusick[7], Abigail R. N. Reynolds[1,2,4], Auriole C. R. Fassinou[1,2,4], Georges Ayoub[7], Seth Malinowski[7], Emily Lapinskas[7], William Pisano[7], John Jeang[1,2,4], Sylwia A. Stopka[12], Michael S. Regan[13], Johan Spetz[14], Arati Desai[15], Frank Lieberman[16], Kamalakannan Palanichamy[17], Joy D. Fisher[8], Kristine Pelton[7], Raymond Y. Huang[12], Kristopher A. Sarosiek[1,18], Louis B. Nabors[19], Matthias Holdhoff[8], Neeraja Danda[20], Roy Strowd[17], Serena Desideri[8], Tobias Walbert[21], Xiaobu Ye[8], Arnab Chakravarti[22], Peter K. Sorger[11], Sandro Santagata[9,11], Nathalie Y. R. Agar[2,12,13], Stuart A. Grossman[8], Brian M. Alexander[23], Patrick Y. Wen[1,3,6]§, Keith L. Ligon[3,4,7,9,24]§, Rameen Beroukhim[1,2,3,4]§

Inhibitors of murine double minute homolog 2 (MDM2) represent a promising therapeutic approach for the treatment of *TP53* wild-type glioblastomas (GBMs), reactivating p53 signaling to induce cancer cell death. We conducted a surgical window-of-opportunity trial (NCT03107780) of the MDM2 inhibitor navtemadlin (KRT-232) in 21 patients with *TP53* wild-type recurrent GBM to determine achievable drug concentrations within tumor tissues and biological mechanisms of response and resistance. Participants received navtemadlin at 120 mg ($n = 10$) or 240 mg ($n = 11$) for 2 days before surgical resection and after surgery until progression or unacceptable toxicity. Both 120 and 240 mg daily dosing achieved a pharmacodynamic impact, but median progression-free survival was 3.1 months. DNA sequencing of three recurrent tumors revealed an absence of *TP53*-inactivating mutations, indicating alternative mechanisms of resistance. To understand the mechanisms of response and resistance associated with navtemadlin, we conducted functional and spatial analyses of human tissue and patient-derived GBM neurosphere models. Navtemadlin induced partial tumor cell death as monotherapy, and combination with temozolomide enhanced apoptosis in GBM neurospheres while sparing normal bone marrow cells in vitro. We also observed up-regulation of oligodendrocyte differentiation genes with navtemadlin treatment and enrichment of oligodendrocyte transcription factor 2 (OLIG2)–positive cells at relapse, suggesting an unexplored mechanism of navtemadlin tolerance in GBM. Overall, these results indicated that clinically achievable doses of navtemadlin exert pharmacodynamic effects on GBM and suggest that combined treatment with temozolomide may be a route to more durable survival benefits.

INTRODUCTION

More than 60% of glioblastomas (GBMs) express wild-type *TP53*, a tumor suppressor gene that controls cell fate decisions in response to intrinsic and extrinsic stimuli such as replicative stress and DNA damage (*1*). TP53 (p53) plays a critical role in preventing cancer development by activating the transcription of numerous genes involved in DNA damage repair, cell cycle arrest, and cell death by apoptosis (*2*). The discovery of the protein-protein interaction between p53 and its negative regulator murine double minute homolog 2 (MDM2) has prompted the design of small-molecule MDM2 inhibitors, including nutlin-3, its various chemical derivatives, and second-generation agents such as KRT-232 (navtemadlin, formerly AMG

[1]Department of Medical Oncology and Center for Neuro-Oncology, Dana-Farber Cancer Institute, Boston, MA 02215, USA. [2]Department of Cancer Biology, Dana-Farber Cancer Institute, Boston, MA 02215, USA. [3]Harvard Medical School, Boston, MA 02115, USA. [4]Broad Institute of MIT and Harvard, Cambridge, MA 02142, USA. [5]Department of Immunology, Genetics and Pathology, Uppsala University, SE-751 05 Uppsala, Sweden. [6]Department of Neurology, Brigham and Women's Hospital, Boston, MA 02115, USA. [7]Department of Pathology, Dana-Farber Cancer Institute, Boston, MA 02215, USA. [8]Sidney Kimmel Comprehensive Cancer Center, Johns Hopkins University School of Medicine, Baltimore, MD 21231, USA. [9]Department of Pathology, Brigham and Women's Hospital, Boston, MA 02115, USA. [10]Department of Biomedical Informatics, University of Pittsburgh, Pittsburgh, PA 15206-3701, USA. [11]Laboratory of Systems Pharmacology, Harvard Medical School, Boston, MA 02115, USA. [12]Department of Neurosurgery, Brigham and Women's Hospital, Harvard Medical School, Boston, MA 02115, USA. [13]Department of Radiology, Brigham and Women's Hospital, Harvard Medical School, Boston, MA 02115, USA. [14]Department of Medical Radiation Sciences, Sahlgrenska Cancer Center, Institute of Clinical Sciences, Sahlgrenska Academy, University of Gothenburg, 405 30 Gothenburg, Sweden. [15]Division of Hematology and Oncology, Perelman School of Medicine, University of Pennsylvania, Philadelphia, PA 19104, USA. [16]Department of Neurology, University of Pittsburgh, Pittsburgh, PA 15213, USA. [17]Department of Neurology, Wake Forest University, Winston-Salem, NC 27157, USA. [18]John B. Little Center for Radiation Sciences, Harvard T. H. Chan School of Public Health, Boston, MA 02115, USA. [19]Department of Neurology, University of Alabama at Birmingham, Birmingham, AL 35233, USA. [20]Division of Hematology, Departments of Medicine and Oncology, Montefiore Medical Center, New York, NY 10467, USA. [21]Department of Neurology and Neurosurgery Henry Ford Health, Department of Neurology, Wayne State University and Michigan State University, Detroit, MI 48201, USA. [22]Department of Radiation Oncology, Ohio State University College of Medicine, Columbus, OH 43210-1228, USA. [23]Department of Radiation Oncology, Brigham and Women's Hospital, Harvard Medical School, Boston, MA 02115, USA. [24]Department of Pathology, Boston Children's Hospital, Boston, MA 02115, USA.
*Corresponding author. Email: veronica.rendo@igp.uu.se (V.R.); eudocia_lee@dfci.harvard.edu (E.Q.L.)
†These authors contributed equally to this work.
‡Deceased.
§These authors contributed equally to this work.

232) (*3*–*5*). Because disruption of the binding of MDM2 to p53 leads to reactivation of p53 signaling in cancer cells, MDM2 inhibition has been deemed a promising therapeutic strategy for the treatment of *TP53* wild-type tumors.

With the development of more potent and blood-brain barrier–penetrant MDM2 inhibitors, new clinical trials are evaluating monotherapy and combination approaches to treat *TP53* wild-type and *MDM2*-amplified solid tumors (*6*–*8*). In the context of high-grade gliomas, MDM2 inhibition has been shown to have both in vitro and in vivo efficacy in patient-derived GBM stem cells, particularly in *TP53* wild-type tumors with *MDM2* or *murine double minute X* (*MDMX*) amplification (*9*–*11*). Navtemadlin is an orally bioavailable, selective small-molecule inhibitor of MDM2 that blocks the protein-protein interaction between MDM2 and p53 with higher affinity than previously tested compounds (*12*). An initial phase I clinical trial evaluated the effect of navtemadlin in patients with advanced solid tumors and multiple myeloma including 10 patients with GBM (*6*), but a comprehensive assessment of brain penetration was not done. Therefore, we sought to perform a surgical window-of-opportunity trial in patients with recurrent GBM. The purpose was to ensure that at least 50% of patients attained sufficient drug concentrations (above 25 nM, the lowest concentration for which benefit in combination with radiation was seen in preclinical in vitro models) in contrast-enhancing brain tissue. This was selected as a more useful alternative measure than a brain-to-plasma ratio cutoff on the basis of the recommendations of the Adult Brain Tumor Consortium (ABTC) (*13*). In addition, non–contrast-enhancing brain tissue was obtained to assess the difference in the concentrations attained.

RESULTS

Design of trial NCT03107780

We performed a phase 0/1 surgical window-of-opportunity trial (NCT03107780) of the MDM2 inhibitor navtemadlin (KRT-232) in patients with GBM in association with the ABTC (#1604) and the National Cancer Institute's (NCI's) Cancer Therapy Evaluation Program (Fig. 1A). In the phase 0 component (a surgical window of opportunity in patients with recurrent GBM), the primary objective was to determine the tumor tissue concentration and variability of navtemadlin exposure. The secondary objectives involved determining the safety and toxicity as well as the pharmacodynamic (PD) effects of navtemadlin on cyclin-dependent kinase inhibitor 1A (*CDKN1A*)/p21 as a readout of p53 pathway engagement. The phase 1 component, a dose-escalation study of navtemadlin plus radiation in patients with newly diagnosed O^6-methylguanine-DNA methyltransferase (*MGMT*) unmethylated, *TP53* wild-type GBM, opened within the Alliance for Clinical Trials in Oncology and is not reported here.

A total of 21 patients with recurrent GBM were enrolled in the surgical window-of-opportunity study from July 2018 to April 2020. These patients received oral navtemadlin at 120 mg ($n = 10$) or 240 mg ($n = 11$; recommended phase 2 dose as monotherapy) daily for 2 days before surgical resection (Fig. 1B). These doses were previously shown (*14*) to increase serum concentrations of the macrophage inhibitory cytokine–1 (MIC-1), a validated biomarker of MDM2 inhibitor effects and a surrogate for p53 reactivation in circulating immune cells. Surgery was performed 3 to 6 hours after the second administration of navtemadlin (equivalent to drug treatment for >30 hours).

Trial outcomes

Baseline patient characteristics are provided in Table 1, with 18 patients diagnosed on central pathology review as having GBM, isocitrate dehydrogenase (*IDH*) wild type, and 2 patients as GBM, *IDH* mutant, as per World Health Organization (WHO) 2016 criteria. We performed regional quantification of tissue components by implementing a deep learning–based convolutional neural network on hematoxylin and eosin (H&E) whole-slide images. On the basis of this quantification, 20% of a viable tumor was deemed sufficient to proceed with the study (fig. S1A). Six patients did not receive navtemadlin after surgery (one elective withdrawal, one with no tumor/pseudoprogression on trial pathology, and four identified as *TP53* mutant on trial pathology). One additional patient with *TP53* mutant disease inadvertently received postoperative treatment with navtemadlin and therefore was included in pharmacokinetic (PK), PD, and safety analyses but was excluded from survival analysis. The one patient with no tumor/pseudoprogression was excluded from clinical results but was retained in the safety summary. Fourteen participants with *TP53* wild-type tumors continued navtemadlin after recovery from surgery at the recommended phase 2 dose of 240 mg daily for 7 days every 3 weeks. Median progression-free survival (PFS) of this surgical cohort ($n = 14$) was 3.1 months [95% confidence interval (CI): 2.4–3.3], and median overall survival (OS) was 10.0 months (95% CI: 7.4–16.3) (Fig. 1C). Overall, navtemadlin was generally well tolerated. Grade 3 or higher adverse events at least possibly related to navtemadlin included one patient each experiencing grade 3 diarrhea, fatigue, lymphocyte decrease, and platelet count decrease and one patient each experiencing grade 4 cerebral edema, neutrophil count decrease, platelet count decrease, and white blood count decrease, as summarized in Table 2. Further Oncopanel-based targeted next-generation sequencing of available tumor tissues ($n = 16$) revealed a proportion of GBMs to exhibit additional amplifications of *epidermal growth factor receptor* (*EGFR*) ($n = 6$) and *MDM2* ($n = 5$) (fig. S1B). Significant increases in overall survival were observed in *TP53* wild-type patients on the basis of *EGFR* ($P = 0.029$) but not *MDM2* ($P = 0.40$) amplification status (fig. S1, B and C).

Pharmacokinetic and pharmacodynamic analyses

The study met the prespecified criteria of ≥25 nM intratumor drug concentrations in more than 50% of the patients for both 120- and 240-mg cohorts in contrast-enhancing regions of tumors. We performed liquid chromatography coupled with tandem mass spectrometry (LC-MS/MS) on contrast-enhancing and non–contrast-enhancing tumor samples on 10 patients each in the 120- and the 240-mg cohorts. In the 120-mg cohort, 80% of patients (8/10) had drug concentrations ≥25 nM with the median being 43.1 ± 39.6 nM in the contrast-enhancing tissues. In the 240-mg cohort, 100% of patients (10/10) had drug concentrations ≥25 nM with a median of 137.4 ± 144.3 nM in the contrast-enhancing tissues (Fig. 1D).

We further evaluated the distribution of navtemadlin in both contrast-enhancing and non–contrast-enhancing regions of the brain using matrix-assisted laser desorption ionization (MALDI) mass spectrometry imaging for 13 patients (Figs. 1E and 2A). This confirmed brain penetration and determined higher navtemadlin concentrations in contrast-enhancing compared with non–contrast-enhancing tissues for some patients. Most patients, however, exhibited similar concentrations between contrast-enhancing and non–contrast-enhancing regions.

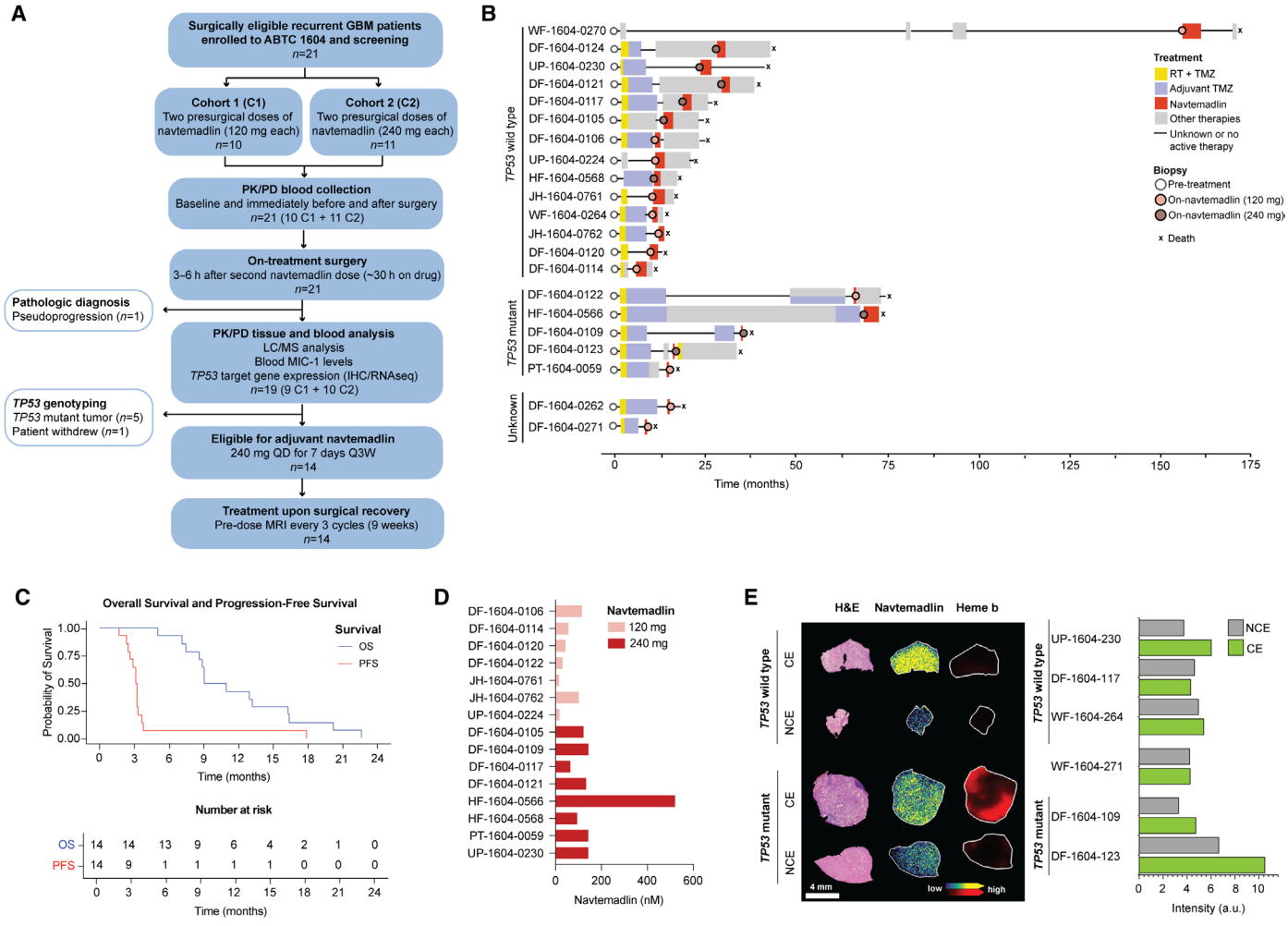

Fig. 1. Schematic for the surgical window-of-opportunity trial and patient outcomes. (**A**) CONSORT diagram demonstrating the overall schematic for the ABTC-1604 clinical trial, which randomized surgically eligible patients with recurrent GBM to receive 120 or 240 mg of navtemadlin daily for 2 days before surgery, followed by surgical resection, followed by 240 mg of navtemadlin daily every 3 weeks after surgery if *TP53* wild-type status was confirmed. (**B**) Timeline for enrolled patients, indicating the duration of radiation plus TMZ (RT + TMZ; yellow), adjuvant TMZ (purple), navtemadlin (red), and other (gray) or unknown (black line) treatments. The first nine patients had pretreatment- and on-navtemadlin–matched biopsies available for downstream analyses. (**C**) Kaplan-Meier curves of OS and PFS in the patient presurgical dose cohorts. (**D**) LC-MS/MS–derived pharmacokinetic data in contrast-enhancing tissues from patients receiving 120 mg ($n = 7$) or 240 mg ($n = 8$) of navtemadlin. (**E**) Microscopy and mass spectrometry images (left) of frozen tissue sections collected from two patients with *TP53* wild-type (UP-1604-0230) and *TP53* mutant (DF-1604-0123) GBM from specimens resected in magnetic resonance imaging contrast-enhancing (CE) and nonenhancing (NCE) tumor regions. Ion images of navtemadlin (*m/z* 301.051) and heme b (*m/z* 616.178) are displayed for each specimen. Bar graph (right) represents the average ion intensity across each tissue section.

PD impact was also achieved in patient blood samples. We assessed the fold change in serum MIC-1 protein concentration by enzyme-linked immunosorbent assay (ELISA), expressed as a fold change relative to baseline (FCB) in 19 patients in the 120- and the 240-mg arms. The fold variability in the two baseline (predose) measurements was 1.1 ± 0.5-fold ($n = 9$) or 1.0 ± 0.1-fold ($n = 10$) at the 120- or 240-mg dose, respectively. Serum MIC-1 FCBs were elevated ~24 hours after a single dose of navtemadlin. In addition, there was evidence of a dose effect on serum MIC-1, given that amounts were two times higher in the 240-mg cohort (7.8 ± 3.9-FCB; $n = 10$) than in the 120-mg cohort (3.5 ± 1.5-FCB; $n = 9$).

Navtemadlin's pharmacodynamic response in patient tumors

To detect whether navtemadlin activates the p53 pathway in patient tumor tissues, we conducted immunohistochemistry and bulk RNA sequencing (RNA-seq) of formalin-fixed paraffin-embedded (FFPE) biopsies obtained at diagnosis (pretreatment) and after 30 hours of drug exposure (on-treatment; on-navtemadlin). Previous studies have shown that MDM2 inhibitors induce *CDKN1A* (p21) RNA and protein; thus, we chose this p53 target as the primary tissue PD end point for the study (*15*). Paired specimens from the same patient were chosen to control for potential patient-to-patient variability in baseline CDKN1A expression. On-treatment surgical tissues were

Table 1. Baseline patient characteristics.

	120-mg group ($n = 10$)	240-mg group ($n = 10$)	Total surgical arm ($n = 20$)
Age			
Median	61	56	59
Range	40–77	34–71	34–77
Sex, *n* (%)			
Male	7 (70)	7 (70)	14 (70)
Female	3 (30)	3 (30)	6 (30)
Race, *n* (%)			
White	10 (100)	10 (100)	20 (100)
KPS, *n* (%)			
90–100	6 (60)	7 (70)	13 (65)
70–80	2 (20)	3 (30)	5 (25)
50–60	2 (20)	0 (0)	2 (10)
Anticonvulsant, *n* (%)			
Yes	7 (70)	7 (70)	14 (70)
No	3 (30)	3 (30)	6 (30)
IDH, *n* (%)			
Mutant	0 (0)	1 (10)	1 (5)
Wild type	9 (90)	9 (90)	18 (90)
Mutant to wild type	1 (10)	0 (0)	1 (5)
MGMT status, *n* (%)			
Methylated	1 (10)	5 (50)	6 (30)
Unmethylated	9 (90)	4 (40)	13 (65)
Not assessed	0 (0)	1 (10)	1 (5)
Prior no. of relapses			
Median (range)	1 (1–2)	1 (1–4)	1 (1–4)
Prior surgical procedure, *n* (%)			
Gross total resection	6 (60)	4 (40)	10 (50)
Subtotal resection	4 (40)	6 (60)	10 (50)
Prior therapy, *n* (%)			
Temozolomide	9 (90)	9 (90)	18 (90)
Other	5 (50)	6 (60)	11 (55)
Steroid usage, *n* (%)			
Yes	4 (40)	2 (20)	6 (30)
No	6 (60)	8 (80)	14 (70)

obtained for all 21 patients; paired pre- and on-treatment tissue sections and evaluable RNA were available from seven and nine *TP53* wild-type patients, respectively (fig. S2B).

Both immunohistochemistry and RNA-seq analyses detected p53 pathway activation in tumor tissue. In immunohistochemistry analyses, we detected a significant increase in the percentage of tumor cells expressing CDKN1A with treatment ($P = 0.01$) as well as a decrease in the proliferative marker Ki67 ($P = 0.05$). Tumor p53 abundance did not vary significantly with treatment ($P = 0.11$; Fig. 2A). We confirmed p53 pathway activation in the RNA-seq data using two separate analyses. First, we compared the expression of known transcriptional targets of p53 involved in feedback mechanisms [*MDM2*, *cyclin-G1* (*CCNG1*), and *protein phosphatase Mg/Mn-dependent 1D* (*PPM1D*)], DNA repair [*DNA damage-binding protein 2* (*DDB2*), *ribonucleotide-diphosphate reductase subunit M2 B* (*RRM2B*), and *proliferating cell nuclear antigen* (*PCNA*)], cell cycle arrest [*B cell translocation gene 2* (*BTG2*), *growth arrest and DNA damage inducible alpha* (*GADD45A*) and *CDKN1A*], and apoptosis [*BCL2-associated X* (*BAX*), *p53 up-regulated modulator of apoptosis* (*PUMA*), and *TP53 regulated inhibitor of apoptosis 1* (*TRIAP1*)] (*2*). We detected significant up-regulation of the cell cycle regulators *CDKN1A* ($P = 0.014$) and *BTG2* ($P = 0.024$) and the DNA repair gene *DDB2* ($P = 0.004$) with navtemadlin treatment; the other targets were unchanged (fig. S2C). *CDKN1A* expression in on-treatment biopsies also showed a positive correlation with PFS [coefficient of determination (R^2) = 0.618; $P = 0.012$], suggesting that *CDKN1A* is a biomarker of p53 pathway activation in this patient cohort (Fig. 2B).

Because enrolled patients had recurrent GBM, most patients had been exposed to other treatments [most commonly standard-of-care (SOC) temozolomide (TMZ) and radiation] after initial diagnosis,

Table 2. Adverse events at least possibly related to navtemadlin. CTCAE, common terminology criteria for adverse events.

Adverse event	Grade 1	Grade 2	Grade 3	Grade 4	Total
CTCAE v.5	***n* (%)**	***n* (%)**	***n* (%)**	***n* (%)**	***n* (%)**
Abdominal pain	1 (4.8)	0 (0.0)	0 (0.0)	0 (0.0)	1 (4.8)
Anemia	5 (23.8)	0 (0.0)	0 (0.0)	0 (0.0)	5 (23.8)
Anorexia	2 (9.5)	2 (9.5)	0 (0.0)	0 (0.0)	4 (19.0)
Atrial fibrillation	1 (4.8)	0 (0.0)	0 (0.0)	0 (0.0)	1 (4.8)
Cerebral edema	1 (4.8)	0 (0.0)	0 (0.0)	1 (4.8)	1 (4.8)
Chills	1 (4.8)	0 (0.0)	0 (0.0)	0 (0.0)	1 (4.8)
Constipation	1 (4.8)	0 (0.0)	0 (0.0)	0 (0.0)	1 (4.8)
Creatinine increased	1 (4.8)	0 (0.0)	0 (0.0)	0 (0.0)	1 (4.8)
Decreased appetite	1 (4.8)	0 (0.0)	0 (0.0)	0 (0.0)	1 (4.8)
Dehydration	0 (0.0)	1 (4.8)	0 (0.0)	0 (0.0)	1 (4.8)
Diarrhea	8 (38.1)	1 (4.8)	1 (4.8)	0 (0.0)	10 (47.6)
Dizziness	1 (4.8)	0 (0.0)	0 (0.0)	0 (0.0)	1 (4.8)
Dry mouth	1 (4.8)	0 (0.0)	0 (0.0)	0 (0.0)	1 (4.8)
Dyspnea	1 (4.8)	0 (0.0)	0 (0.0)	0 (0.0)	1 (4.8)
Fatigue	2 (9.5)	4 (19.0)	1 (4.8)	0 (0.0)	7 (33.3)
Fecal incontinence	1 (4.8)	0 (0.0)	0 (0.0)	0 (0.0)	1 (4.8)
Flatulence	1 (4.8)	0 (0.0)	0 (0.0)	0 (0.0)	1 (4.8)
Generalized muscle weakness	1 (4.8)	0 (0.0)	0 (0.0)	0 (0.0)	1 (4.8)
Groin rash	0 (0.0)	1 (4.8)	0 (0.0)	0 (0.0)	1 (4.8)
Headache	0 (0.0)	2 (9.5)	0 (0.0)	0 (0.0)	2 (9.5)
Hiccups	0 (0.0)	1 (4.8)	0 (0.0)	0 (0.0)	1 (4.8)
Hyperglycemia	1 (4.8)	0 (0.0)	0 (0.0)	0 (0.0)	1 (4.8)
Hyperphosphatemia	1 (4.8)	0 (0.0)	0 (0.0)	0 (0.0)	1 (4.8)
Hypertension	0 (0.0)	1 (4.8)	0 (0.0)	0 (0.0)	1 (4.8)
Hypoalbuminemia	1 (4.8)	0 (0.0)	0 (0.0)	0 (0.0)	1 (4.8)
Hypocalcemia	2 (9.5)	0 (0.0)	0 (0.0)	0 (0.0)	2 (9.5)
Hypokalemia	4 (19.0)	0 (0.0)	0 (0.0)	0 (0.0)	4 (19.0)
Hyponatremia	1 (4.8)	0 (0.0)	0 (0.0)	0 (0.0)	1 (4.8)
Hypophosphatemia	1 (4.8)	0 (0.0)	0 (0.0)	0 (0.0)	1 (4.8)
Lymphocyte count decreased	2 (9.5)	1 (4.8)	1 (4.8)	0 (0.0)	4 (19.0)
Nausea	5 (23.8)	4 (19.0)	0 (0.0)	0 (0.0)	9 (42.9)
Neutrophil count decreased	3 (14.3)	1 (4.8)	0 (0.0)	1 (4.8)	5 (23.8)
Pain of skin	0 (0.0)	1 (4.8)	0 (0.0)	0 (0.0)	1 (4.8)
Peripheral sensory neuropathy	1 (4.8)	0 (0.0)	0 (0.0)	0 (0.0)	1 (4.8)
Platelet count decreased	8 (38.1)	1 (4.8)	1 (4.8)	1 (4.8)	11 (52.4)
Stomach pain	1 (4.8)	0 (0.0)	0 (0.0)	0 (0.0)	1 (4.8)
Tinnitus	0 (0.0)	1 (4.8)	0 (0.0)	0 (0.0)	1 (4.8)
Vomiting	2 (9.5)	2 (9.5)	0 (0.0)	0 (0.0)	4 (19.0)
Weight gain	1 (4.8)	0 (0.0)	0 (0.0)	0 (0.0)	1 (4.8)
White blood cell decreased	8 (38.1)	2 (9.5)	0 (0.0)	1 (4.8)	11 (52.4)

before collection of their pretreatment biopsies. To control for potential confounding effects of other treatments in on-treatment navtemadlin samples, we analyzed RNA-seq data from an independent cohort of 25 *TP53* wild-type and *IDH* wild-type GBM tissue sample pairs obtained before and after SOC treatments with TMZ and radiation, profiled by the Glioma Longitudinal Analysis (GLASS) consortium (https://glass-consortium.org) (fig. S2D). No up-regulation of p53 transcriptional targets was identified in these

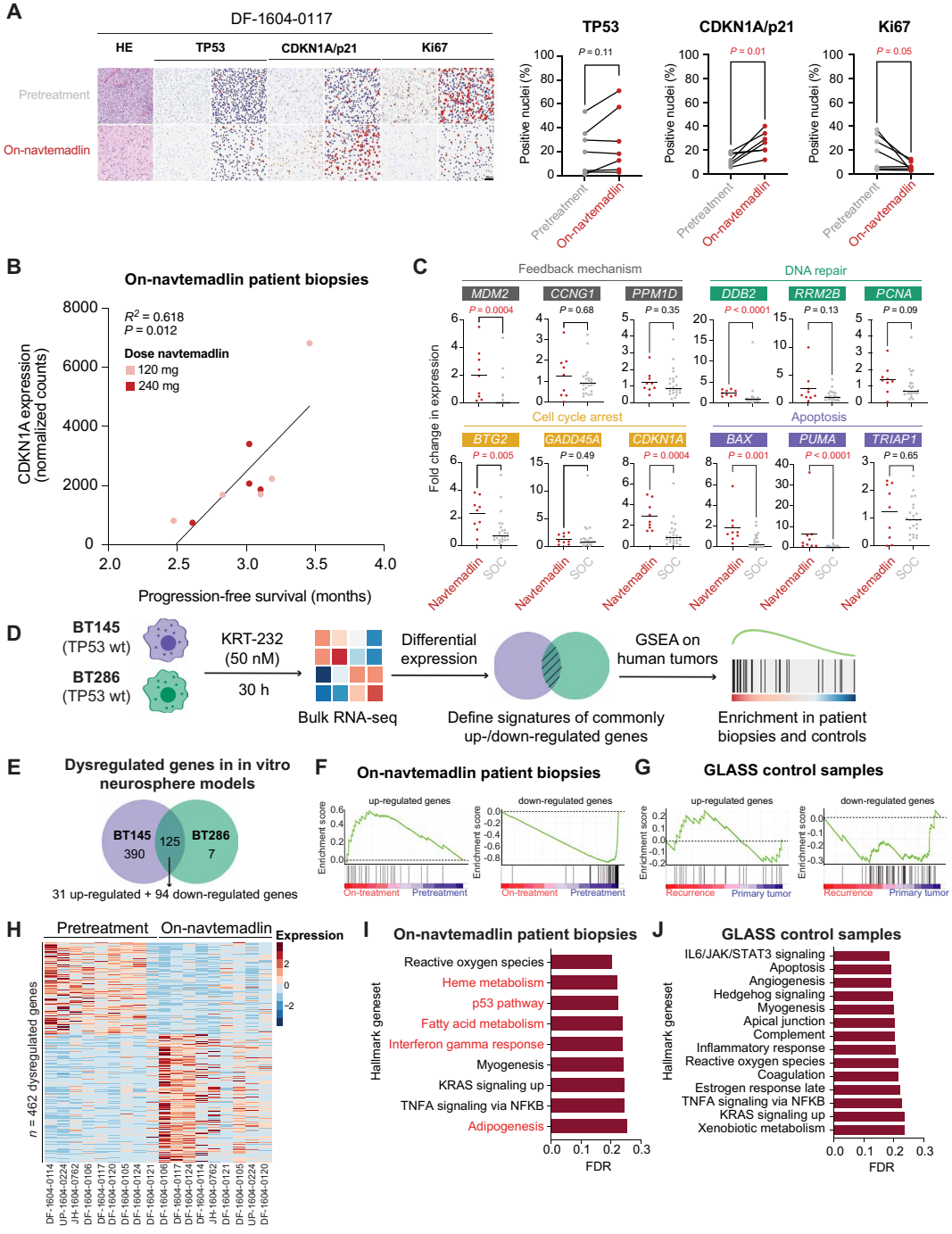

Fig. 2. Evaluation of navtemadlin's pharmacodynamic response in patient tumors. (**A**) Representative H&E and immunohistochemistry staining for TP53, CDKN1A, and Ki67 (left) and quantification of positive nuclei in pretreatment and on-navtemadlin tumor samples (right). Percentages of tumor cells expressing p53, CDKN1A, and Ki67 are shown, as determined by the quantification of positive nuclei from whole-slide immunohistochemistry images at 40× magnification. Scale bar, 50 μm. (**B**) Correlation between *CDKN1A* gene expression and PFS. The R^2 value was calculated by Pearson correlation with a 95% CI (two-tailed *P* value). (**C**) Fold change in expression of *TP53* transcriptional targets in on-navtemadlin patient biopsies (red; on-treatment versus pretreatment sample) and SOC-treated GLASS control samples (gray; recurrence versus primary tumor sample). Data were analyzed with a Wilcoxon rank sum test. (**D**) Schematic representation of the RNA-seq experiments. In vitro signatures of p53 pathway activation were created by bulk RNA-seq of two *TP53* wild-type GBM cell lines. GSEA was performed to examine enrichment in pre- and on-treatment patient biopsies and controls. (**E**) Differential expression analysis and commonly dysregulated genes in BT145 and BT286 cells. (**F**) Enrichment of on-navtemadlin patient biopsies for p53 pathway signatures. (**G**) Enrichment of GLASS control samples for p53 pathway signatures. (**H**) Dysregulated genes in pretreatment and on-treatment patient biopsies. Differential gene expression was determined with cutoffs of FDR 5% and $\log_2$ fold change ±1. (**I** and **J**) GSEA for (I) on-navtemadlin patient biopsies and (J) GLASS control samples using hallmark gene sets. Pathways enriched with navtemadlin treatment and not present in SOC controls are shown in red.

posttreatment samples (fig. S2E). When comparing increases in expression of each p53 transcriptional target between our clinical trial and GLASS control samples, we observed significant up-regulation of *MDM2* ($P = 0.0004$), *CDKN1A* ($P = 0.0004$), *BTG2* ($P = 0.005$), *DDB2* ($P < 0.0001$), *BAX* ($P = 0.001$), and *PUMA* ($P < 0.0001$) in navtemadlin-treated samples (Fig. 2C), suggesting a treatment-specific effect. Of these canonical targets, *CDKN1A* exhibited the highest change in response to navtemadlin after ~30 hours of treatment.

We detected similar PD effects in preclinical studies at similar drug concentrations. We performed RNA-seq of two patient-derived in vitro neurosphere models (BT145 and BT286), both pre- and on-treatment with navtemadlin at an equivalent dose and time point to the clinical trial (Fig. 2D). We detected altered expression of 390 and 132 genes in BT145 and BT286, respectively, with 125 genes common to both ($P < 0.0001$) (Fig. 2E). We used these 125 genes to construct sets of genes expected to be up-regulated ($n = 31$) and down-regulated ($n = 94$) by treatment and applied these gene sets to the RNA-seq data from our clinical trial samples. We found on-treatment samples to be enriched for the up-regulated genes ($P = 0.030$), whereas pretreatment samples were enriched for the down-regulated genes ($P < 0.001$) (Fig. 2F). In contrast, analysis of samples from the GLASS dataset revealed no enrichment for up-regulated ($P = 0.727$) or down-regulated ($P = 0.647$) genes after SOC treatment (Fig. 2G), suggesting that navtemadlin exhibited PD activity in human GBMs.

We also explored other pathways that were altered by navtemadlin. Using a false discovery rate (FDR) cutoff of 5%, we detected a total of 462 significantly dysregulated genes (Fig. 2H). Among the 50 Molecular Signatures Database (MSigDB) hallmark gene sets (*16*), none reached an FDR threshold of 5%. The most significantly altered gene sets reflected regulation of reactive oxygen species and cell metabolism, with the hallmark p53 pathway ranking third (FDR = 22.4%; Fig. 2I). However, we did not observe dysregulation of the p53 pathway in SOC-treated control GLASS samples, suggesting that this enrichment is specific to treatment with navtemadlin (Fig. 2J).

To further understand the PD effects of navtemadlin, we performed tissue-based cyclic immunofluorescence (t-CyCIF) on paired pre- and on-treatment biopsies from eight patients and stratified the patients by their *MDM2* and *TP53* status. Immunofluorescence imaging of multiple markers in situ in the same section of tumor tissue allowed us to perform cell phenotyping and examination of navtemadlin treatment changes specifically on tumor cells (fig. S3, A to D). This analysis also confirmed p53 pathway activation with on-treatment biopsies having a lower percentage of $Ki67^+$ tumor cells (fig. S3E) and a larger percentage of $p53^+$ and $p21^+$ tumor cells (fig. S4, A and B). Examining the changes in each patient individually revealed the largest effect on *MDM2* wild-type, *TP53* wild-type patients (fig. S4, C to E), with the greatest changes in p53 and MDM2 protein being detected in the on-treatment biopsies.

We then compared the ratios of proliferative and arrested cells within individual tumors and represented the data using the Arrested to Proliferative Index, which allowed us to quantify and visualize the flux of these two dynamic processes in pre- versus on-treatment biopsies. *MDM2* wild-type, *TP53* wild-type patients had the greatest shift toward an arrested state when treated with navtemadlin (fig. S5, A and B), whereas *MDM2* wild-type, *TP53*-mutated tumors shifted toward a more proliferative state, and *MDM2*-amplified, *TP53* wild-type tumors exhibited mixed responses.

Cellular effects of navtemadlin treatment in patient-derived GBM models

Despite the up-regulation of *TP53* transcriptional targets, we did not observe evidence that p53 pathway inactivation contributed to tumor recurrence. Because direct inactivation of p53 by mutation or deletion is a known resistance mechanism to MDM2 inhibition (*17*), we sequenced *TP53* in three posttreatment tumors obtained from three patients who underwent biopsies at recurrence. However, we detected no accumulation of p53 protein by immunohistochemistry, suggesting that no inactivating mutations were acquired in on-treatment or posttreatment biopsies (Fig. 3A).

To understand how tumors could recur in the absence of direct inactivation of *TP53*, we explored the effects of clinically relevant concentrations of navtemadlin on cell growth, viability, and p53 pathway activity in both *TP53* wild-type (BT145 and BT286) and *TP53* mutant (BT359) patient-derived neurosphere lines. First, we generated dose-response curves at 72 hours of treatment, which showed that the *TP53* wild-type lines are more sensitive than the *TP53* mutant line (Fig. 3B). However, we did observe differences between BT145 and BT286. For example, at the concentration of 50 nM navtemadlin (representative of the lower drug concentration range found in the 120-mg cohort), we observed a >60% decrease in viability for BT286 cells but minimal response for BT145. Protein expression of PUMA (which is involved in apoptosis) but not CDKN1A correlated with this response. With 50 nM navtemadlin, we detected PUMA activation by 6 hours into treatment in BT286 cells, but BT145 cells did not exhibit substantial increases in PUMA until 12 hours after treatment (Fig. 3C). In contrast, CDKN1A up-regulation occurred in both *TP53* wild-type cell lines to a near-equal extent within 6 hours of treatment. Measurements of navtemadlin sensitivity in 16 additional cell line models derived from GBM patients with varying *TP53*, *EGFR*, *CDKN2A*, and *phosphatidylinositol-4,5-bisphosphate 3-kinase catalytic subunit alpha* (*PIK3CA*) status (fig. S6A) suggested that these additional genetic features did not modulate drug response (fig. S6B), with *TP53* mutational status remaining the only statistically significant ($P = 0.0178$) determinant of navtemadlin sensitivity (fig. S6C). Given the risk of MDM2 inhibition to bone marrow and other tissues with rapidly dividing cells (*15*, *18*, *19*), we separately included immortalized bone marrow mesenchymal cells (BMMCs; T0523) in our 72-hour navtemadlin dose-response study. We also characterized drug sensitivity profiles for human immortalized astrocytes (hAstro) and human neural stem cells (hNSCs) to represent normal brain cell populations (Fig. 3B). BMMCs exhibited intermediate sensitivity to MDM2 inhibition, with large decreases in viability observed only with >1000 nM navtemadlin. Moreover, this decrease in viability resolved with removal of the drug, even at very high doses of navtemadlin. We treated BMMCs for 5 days with increasing concentrations of navtemadlin and monitored cell confluency over time by live-cell imaging. Treatment with as little as 10 nM navtemadlin caused growth inhibition, with the strongest phenotypes being observed at >500 nM (Fig. 3D). However, when we washed out navtemadlin from the media, we observed a resumption of growth to confluency among all conditions up to 5000 nM—a 35-fold higher concentration of navtemadlin compared with the 140 nM median achieved in the resected brain tumors from patients treated with the higher 240-mg dose. At 6 days into treatment with continuous doses of 50 nM navtemadlin, flow cytometry for annexin V and propidium iodide (PI) detected increased apoptosis relative to DMSO controls in both

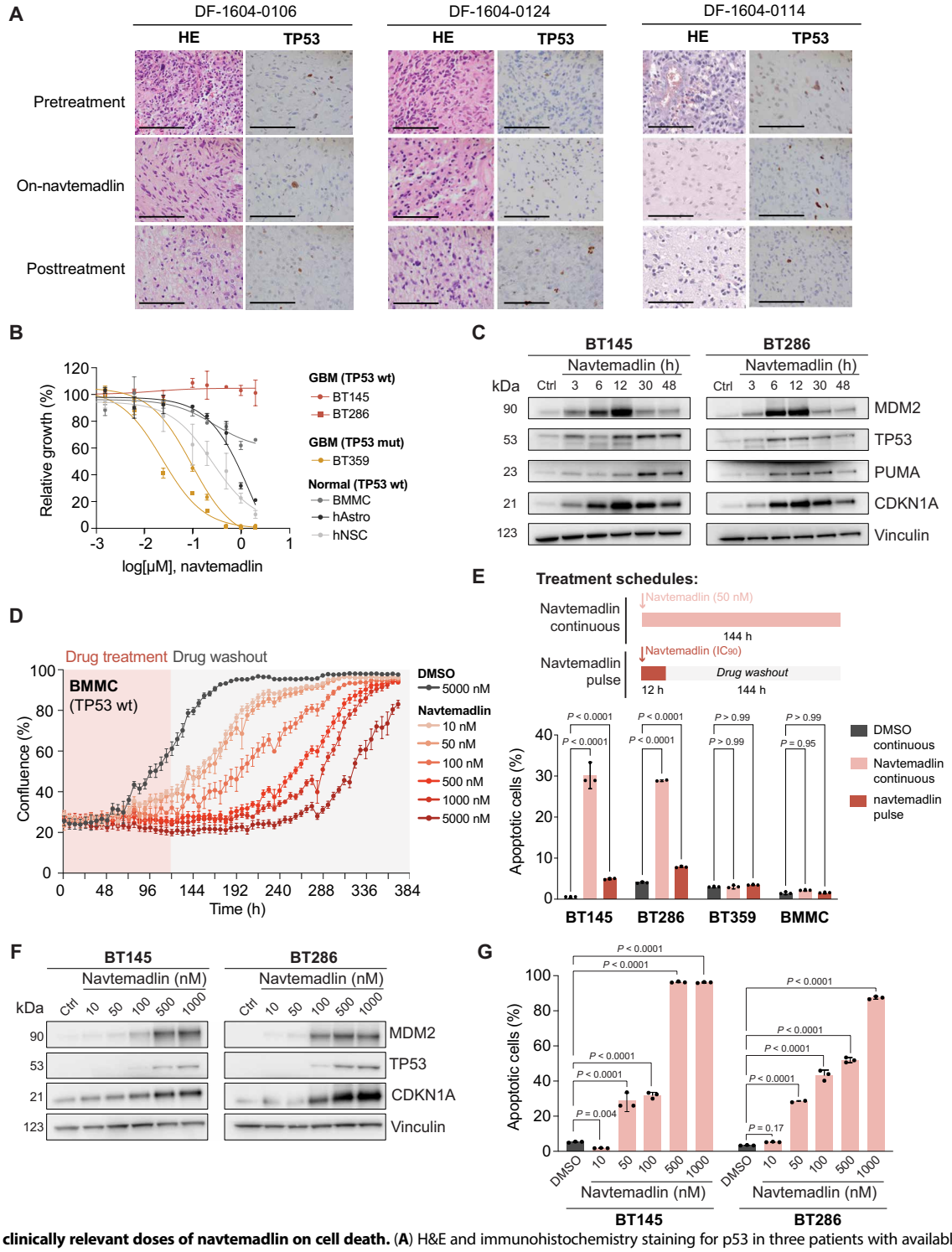

Fig. 3. Effect of clinically relevant doses of navtemadlin on cell death. (**A**) H&E and immunohistochemistry staining for p53 in three patients with available pretreatment, on-treatment, and posttreatment biopsy samples. Whole-slide images were selected for quantification at 40× magnification. Scale bars, 100 μm. (**B**) Dose-response curves showing sensitivity of *TP53* wild-type GBM cells (BT145 and BT286; yellow), *TP53* mutant GBM cells (BT359; red), BMMCs (gray), hAstro (dark gray), and hNSCs (light gray) to navtemadlin. (**C**) Immunoblotting of BT145 and BT286 cells treated with 50 nM navtemadlin over the indicated times, for MDM2, TP53, PUMA, and CDKN1A. Vinculin was included as a loading control. (**D**) Growth of BMMCs in response to navtemadlin treatment. Growth phenotypes are shown under treatment with 50 to 5000 nM navtemadlin (red box) and drug washout from media (gray box). (**E**) Effects of continuous (light red) or single-pulse (dark red) navtemadlin treatment modalities on cell death. For the single-pulse modality, tested navtemadlin concentrations were as follows: 100 nM in BT145, 75 nM in BT286, and 500 nM in BT359 and BMMCs. Apoptosis was quantified by annexin V/PI staining. Data were analyzed by two-way ANOVA followed by Dunnett posttest. (**F**) Immunoblotting of BT145 and BT286 cells treated with increasing concentrations of navtemadlin over 72 hours, for MDM2, TP53, and CDKN1A. Vinculin was included as a loading control. (**G**) Effects of increasing concentrations of navtemadlin on tumor cell death. Apoptosis was quantified by annexin V/PI staining after 72 hours of continuous drug treatment. Data were analyzed by two-way ANOVA followed by Dunnett posttest.

TP53 wild-type lines, but not the *TP53* mutant BT359 line or the BMMC line (Fig. 3E and fig. S6, D and E). Unexpectedly, pulsed dosing at the 90% inhibitory concentration (IC_{90}) did not increase the fraction of apoptotic cells in any of our models at 6 days after a 12-hour treatment pulse. These data suggested that the observed suppression in growth among BMMCs reflected growth inhibition rather than apoptosis, further supporting evidence of a therapeutic window between *TP53* wild-type gliomas and normal cells.

However, we did not observe complete ablation of *TP53* wild-type GBM cells at concentrations lower than 500 nM. To further understand the dose of navtemadlin that would be required for increased p53 pathway activation and cell death, we performed a comprehensive functional characterization of our *TP53* wild-type preclinical models after treatment with a wide range of inhibitor concentrations. First, we measured CDKN1A protein expression by immunoblotting as a marker of p53 pathway activation (Fig. 3F) and determined that at least 500 nM navtemadlin was required for robust protein expression. At this concentration, we observed an increase in MDM2 and p53 abundance, in agreement with navtemadlin's role as an MDM2-p53 antagonist (*15*, *20*). By performing flow cytometry–based apoptosis analysis of these cells, we confirmed that 500 nM navtemadlin was required to achieve at least 60% of cell death by apoptosis. Complete cell death in both cell lines was only achieved when treating with 1000 nM navtemadlin (Fig. 3G).

We considered two alternatives to increase rates of cancer cell death after navtemadlin treatment. First, we asked whether a pulsed high dose would induce more cell death than continuous dosing. A previous study suggested that pulsed 80% inhibitory concentration (IC_{80}) doses of an MDM2 inhibitor (siremadlin; HDM-201) enhanced apoptotic signaling over continuous dosing (*21*). We tested single pulses at the following navtemadlin concentrations: 100 nM for BT145, 75 nM for BT286, and 500 nM for BT359 and BMMCs. To further characterize the mechanism by which continuous navtemadlin treatment may induce cell death in glioma cells, we conducted an analysis of BH3 mimetics (*22*) in *TP53* wild-type and mutant GBM cell lines after drug treatment (50 nM for 30 hours). Here, we measured apoptotic priming by determining the fraction of cells that release cytochrome c after incubation with different activator and sensitizer BH3 peptides (fig. S6F). We detected increases in the percentages of cytochrome c–negative navtemadlin-treated BT286 cells and, to some extent, BT145 cells, after incubation with the activator BH3 peptides Bcl-2 interacting mediator of cell death and BH3 interacting domain death agonist treatment, suggesting that MDM2 inhibition does increase apoptotic priming in *TP53* wild-type cells albeit with a limited capacity. No changes in apoptotic priming were observed for mutant BT359 cells. We therefore concluded that continuous low-dose navtemadlin treatment caused more GBM cell death than a pulsed high-dose regimen and that the limited cell death phenotype observed for navtemadlin at the current dosing conditions was explained by partial increases in cellular apoptotic priming present in *TP53* wild-type GBM cells.

Cell death rates associated with dual treatment of navtemadlin and TMZ

As a second alternative to continuous dosing of navtemadlin monotherapy, we explored whether we could enhance its apoptotic effects by applying it in combination with a DNA-damaging agent. Because the ongoing, second phase of this trial is already testing navtemadlin in combination with radiation, we decided to explore combined treatment with TMZ. TMZ is an alkylating agent that preferentially damages DNA in GBMs lacking expression of the DNA repair protein MGMT, usually because of *MGMT* promoter methylation, and is a component of first-line treatment for these tumors. We hypothesized that the replication stress caused by TMZ-induced DNA damage would sensitize cells to p53 pathway activation by navtemadlin. TMZ and navtemadlin have been found to have nonoverlapping mechanisms of action and have been described as synergistic in the context of traditional (nonneurosphere) glioma cell lines (*23*, *24*).

Treatment with both agents for 160 hours caused a reduction in cell growth ($P < 0.0001$) for BT145 and BT286 (*TP53* wild type and *MGMT*-methylated) but not BT359 (*TP53* mutant and *MGMT* unmethylated) cells (Fig. 4A and fig. S7A). In sensitive cell lines, a highest single agent (HSA) model found dual treatment with navtemadlin and TMZ to be synergistic for growth inhibition (fig. S7B). The combined treatment led to increased abundance of MDM2 and p53 at late time points (>30 hours) relative to navtemadlin alone. CDKN1A expression was modestly increased in BT286 with combination treatment, but not in BT145 (Fig. 4B). Flow cytometry for annexin V and PI confirmed increased rates of apoptosis in BT145 and BT286 *TP53* wild-type cells after dual treatment, and in BT286 cells, where sensitivity to TMZ treatment was the highest, the addition of navtemadlin increased cell death across the tested concentration range (Fig. 4C). In contrast, less than 5% cell death was observed in BT359 *TP53* mutant tumor cells or BMMCs, suggesting that the combination of navtemadlin and TMZ retains a therapeutic window for the treatment of *TP53* wild-type and *MGMT*-methylated GBMs (Fig. 4C and fig. S7C).

Among *MGMT*-methylated GBMs, a primary resistance mechanism to TMZ treatment is loss of genes involved in DNA mismatch repair (MMR) (*25*). We engineered isogenic versions of the *MGMT*-methylated BT145 GBM neurospheres both with and without each of the MMR components *MutL protein homolog 1* (*MLH1*) and *MutS homolog 2* (*MSH2*). As expected, MMR loss led to TMZ resistance (Fig. 4D). However, genetic ablation of MMR genes led to only a slight decrease in sensitivity to navtemadlin, and these cells remained markedly more sensitive to navtemadlin than an isogenic *TP53*-null BT145 cell model (Fig. 4E). In a proliferation experiment, we confirmed that tumor cells that become resistant to TMZ via MMR loss retained sensitivity to navtemadlin but no longer benefited from combined navtemadlin and TMZ treatment (fig. S7D). We therefore confirmed that navtemadlin and TMZ exhibited different mechanisms of action and that resistance to TMZ did not necessarily lead to resistance to navtemadlin.

Adaptive changes in cell state associated with navtemadlin treatment

We also investigated whether adaptive changes in cell state contributed to navtemadlin resistance. A previous study has shown that inducing differentiation through exogenous expression of *oligodendrocyte transcription factor 2* (*OLIG2*) decreases sensitivity to MDM2 inhibitors (*26*). We first interrogated our bulk RNA-seq data from the nine patients with *TP53* wild-type tumors that were treated with navtemadlin. Relative to pretreatment samples, on-treatment samples exhibited significant up-regulation (adjusted *P* value <0.05) of genes associated with the GO term "oligodendrocyte differentiation" (GO:0048709), including *proteolipid protein 1* (*PLP1*), *NK6 homeobox 2* (*NKX6-2*), *oligodendrocytic myelin paranodal and inner loop protein* (*OPALIN*), *tubulin polymerization-promoting protein* (*TPPP*), *histone deacetylase*

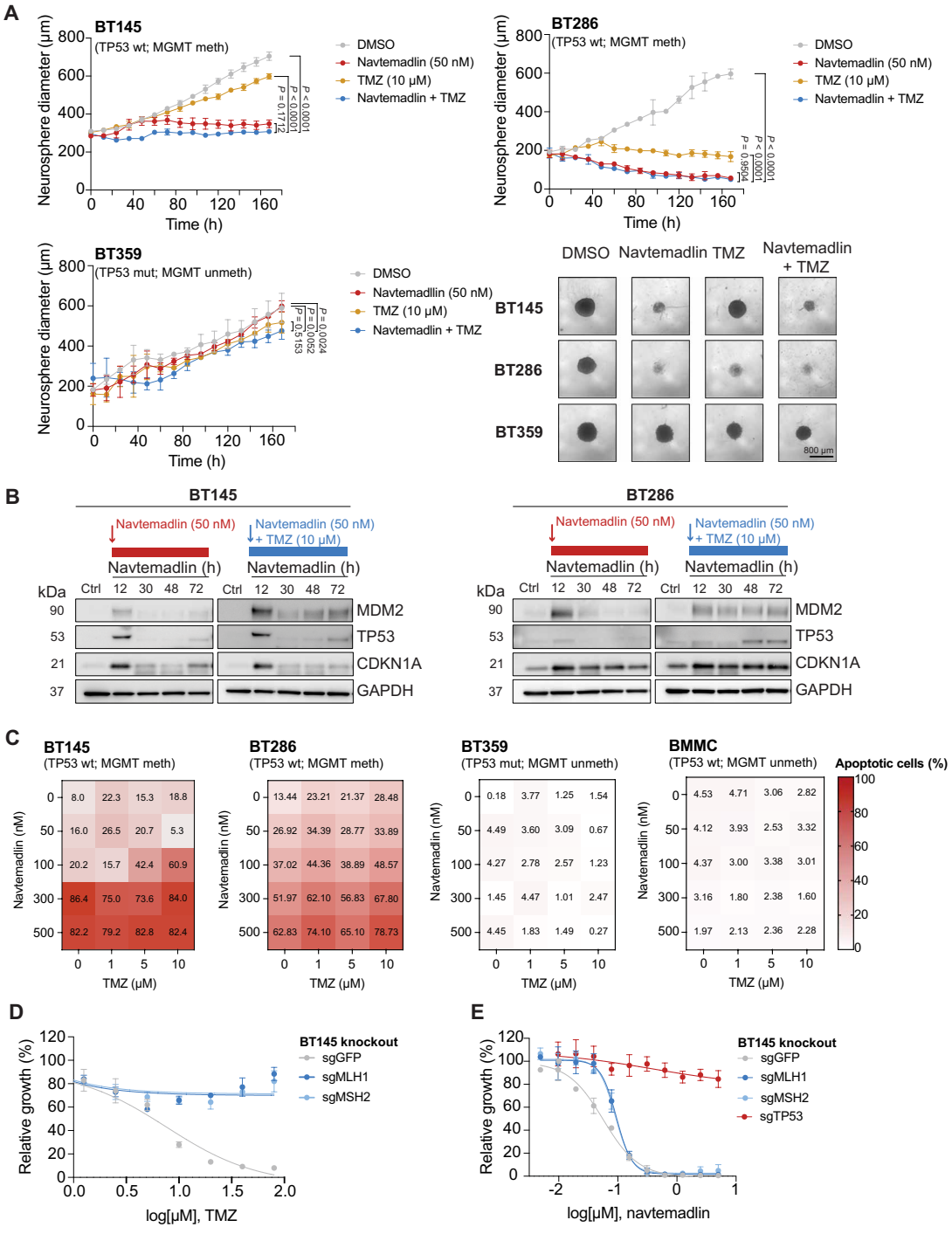

Fig. 4. Effect of combination therapy with navtemadlin and TMZ on cell death rates. (**A**) (Top row) Growth of TP53 wild-type BT145 and BT286 cells when treated continuously with navtemadlin or TMZ as monotherapy or in combination. (Bottom left) Growth of TP53 mutant BT359 cells was performed as control. Mean and SD of three technical replicates shown. Neurosphere diameter was quantified by live imaging over the course of 160 hours for cells treated with navtemadlin (red), TMZ (yellow), or combination therapy (blue). Data were analyzed by two-way ANOVA followed by Dunnett posttest (bottom right). Representative images of TP53 wild-type (BT145 and BT286) and TP53 mutant cells treated for each condition are shown. Scale bar, 800 µm. (**B**) Immunoblot of BT145 (left) and BT286 (right) cells treated with navtemadlin as monotherapy or in combination with TMZ for up to 72 hours for MDM2, TP53, and CDKN1A. GAPDH was included as a loading control. (**C**) Effect of navtemadlin and TMZ combination treatment on TP53 wild-type BT145 and BT286 cells, TP53 mutant BT359 cells, and normal control BMMCs. The percentage of apoptotic cells was calculated by an annexin V/PI flow cytometry assay. (**D** and **E**) Dose-response curves showing the sensitivity of BT145 MLH1 and MSH2 knockout cells to treatment with (D) TMZ and (E) navtemadlin. A GFP sgRNA was used as a CRISPR-Cas9 targeting control. Mean and SD of three technical replicates shown.

11 (*HDAC11*), *dishevelled associated activator of morphogenesis 2* (*DAAM2*), *myelin and lymphocyte protein* (*MAL*), *2′,3′-cyclic nucleotide 3′ phosphodiesterase* (*CNP*), *solute carrier family 45 member 3* (*SLC45A3*), *potassium inwardly rectifying channel subfamily J member 10* (*KCNJ10*), *adenosine triphosphate* (*ATP*) *binding cassette subfamily A member 2* (*ABCA2*), and *contactin-associated protein* (*CNTNAP*) (Fig. 5A). We also used signatures associated with developmental and oncogenic programs developed in a previous analysis of high-grade gliomas (*27*) to interrogate these data using gene set enrichment analysis (GSEA). On-treatment biopsies were enriched for astrocyte-like and oligodendrocyte-like differentiation programs ($P < 0.001$) but depleted of the "cell cycle" signature ($P < 0.001$) (Fig. 5B). In contrast, we did not observe enrichment for these signatures when analyzing GLASS control samples ($P = 0.407$ and $P = 0.690$ for astrocyte-like and oligodendrocyte-like, respectively), nor could we detect a decrease in cycling cells ($P = 0.551$) (Fig. 5C). To further determine whether the oligodendrocyte differentiation signature becomes enriched in tumor cells that survive navtemadlin treatment, we first performed single-sample GSEA (ssGSEA) on RNA-seq data from patient-matched pre-, on-, and posttreatment samples for two patients (DF-1604-0106 and DF-1604-0114) with available tissues (Fig. 5D). Here, we observed a consistent increase in the signature ssGSEA score for both patients, suggesting that up-regulation of these genes persists after navtemadlin treatment. Second, we quantified by immunohistochemistry the fraction of tumor cells positive for OLIG2, a transcription factor mediating differentiation of neural stem cells down the oligodendrocyte lineage (*28*) (Fig. 5E). This analysis confirmed an increase in OLIG2-positive tumor cells in patient relapse samples.

To get better resolution into the effects of navtemadlin on the proportion of different cell types and pathways active in each, we also performed single-cell RNA-seq of BT145 cells treated with 50 nM navtemadlin versus DMSO control for 15 hours (Fig. 5F). Using the Leiden algorithm (*29*), we detected seven clusters (clusters 0 to 6), four of which represent oligodendrocyte precursor (clusters 1, 4, and 6) and more differentiated oligodendrocyte cells (cluster 3), one expressing neuronal markers (cluster 5), and two clusters expressing high expression of histone and cell division genes (clusters 0 and 2). MDM2 inhibition led to a decrease in dividing cells (clusters 0 and 2) as well as an increase in oligodendrocyte-like cells (cluster 3) (Fig. 5G). Cluster 3 was characterized by high expression of genes involved in p53 signaling [e.g., *MAX dimerization protein 4* (*MXD4*), *DNA damage inducible transcript 4* (*DDIT4*), *BTG anti-proliferation factor 1* (*BTG1*), *BTG anti-proliferation factor 2* (*BTG2*), and *receptor for activated C kinase 1* (*RACK1*)], apoptotic cell death [e.g., *BCL2 binding component 3* (*BBC3*), *purinergic receptor P2X 7* (*P2RX7*), *programmed cell death 4* (*PDCD4*), *phosphoinositide-3-kinase regulatory subunit 3* (*PIK3R3*), *SRY-box transcription factor 4* (*SOX4*), and *rho guanine nucleotide exchange factor 7* (*ARHGEF7*)], and development [e.g., *lysine demethylase 5B* (*KDM5B*), *inhibitor of DNA binding 4* (*ID4*), and *synaptotagmin 1* (*SYT1*)] (Fig. 5H). When we projected signatures of p53 pathway activation on uniform manifold approximation and projection (UMAP) visualizations of our data (Fig. 5, I and J), we identified enrichment in cluster 3 ($P = 2.2 \times 10^{-16}$; Fig. 5I). This same subset of cells was marked by high expression of the oligodendrocyte differentiation signature used to analyze our on-treatment human tumor biopsies ($P = 2.2 \times 10^{-16}$) (Fig. 5J). We therefore concluded that navtemadlin induced a PD response that was detectable at the single-cell level and involved increased expression of an oligodendrocyte differentiation signature.

DISCUSSION

In this surgical window-of-opportunity trial in 21 patients with recurrent GBM, the primary end point of drug penetration into tumor tissue was met in both the 120-mg cohort and the 240-mg cohort. Navtemadlin was tolerable with expected toxicities (*6*). The study also showed that navtemadlin penetrated both contrast-enhancing and non–contrast-enhancing tumor tissues and exerted a PD effect. Although the study was not powered to evaluate survival outcomes, PFS and OS were similar to historical controls (PFS of 1.5 to 6 months and OS of 2 to 9 months) (*30*).

Increased use of tissue sampling during glioma clinical trials has recently been advocated (*31*); this study supports its utility. In general, a lack of response may reflect the inability of the treatment to reach cancer cells, lack of a direct PD response on the therapeutic target, lack of cancer cell killing, acquisition of resistance among a minor cell population, or a combination of these factors. We were able to use on- and posttreatment biopsies, combined with an in vitro evaluation of navtemadlin in patient cell lines, to address these possibilities. By detecting a PD response without sufficient cell killing, we can focus on the most promising paths to improving the use of MDM2 inhibitors like navtemadlin in future trials.

Although the apoptosis markers *BAX* and *BBC3*/*PUMA* were expressed in posttreatment biopsies, increased activation of apoptosis is likely necessary for durable clinical benefits. One approach might be to increase on-target inhibition: In vitro studies with representative *TP53* wild-type GBM neurosphere models showed dose-dependent increases in apoptosis and the up-regulation of p53-mediated pathways in multiple populations defined by single-cell RNA-seq, with nearly 100% cell death at 1000 nM concentrations.

We also observed adaptive changes in the cell differentiation state with 50 nM navtemadlin, as evidenced by the up-regulation of genes involved in oligodendrocyte differentiation, along with a decrease in dividing cell clusters. Tumor RNA-seq also demonstrated that genes associated with oligodendrocyte differentiation were among the significantly affected genes in the resected tumor tissues after about 30 hours of navtemadlin treatment, with enrichment scores for both astrocytic-like (AC-like) and oligodendrocytic-like (OC-like) gene sets. High-grade gliomas can adapt to therapeutic pressures by acquiring genetic or transcriptional alterations that modify their cell state (*27*, *32*–*34*). Decreased expression of GBM stemness markers has been observed in patient-derived in vitro cell line spheroids treated with navtemadlin (*10*). However, this represents the first clinical study in any disease to detect such adaptive changes in human tumor tissue treated with MDM2 inhibitors. Previous studies have indicated that progenitor-like cell states among GBM cells promote resistance to TMZ, radiation, and other treatment approaches such as immunotherapy (*35*–*38*). The relative resistance of stem-like cells to standard radiation and TMZ versus the induction of signatures of more differentiated cells by p53 reactivation supports the concept of combining these treatment modalities.

Such combinations of DNA-damaging treatments with targeted p53 pathway activation may also increase rates of cancer cell death. Our preclinical analyses in GBM models revealed that the lower range of clinically relevant navtemadlin concentrations in patient contrast-enhancing and non–contrast-enhancing tissues activates the p53 pathway—including apoptotic signaling—but is insufficient to fully kill the cancer cell population in vitro. A strategy to overcome partial cell death is increasing the dose of the MDM2 inhibitor while accounting for toxicity in normal treatment-sensitive tissues.

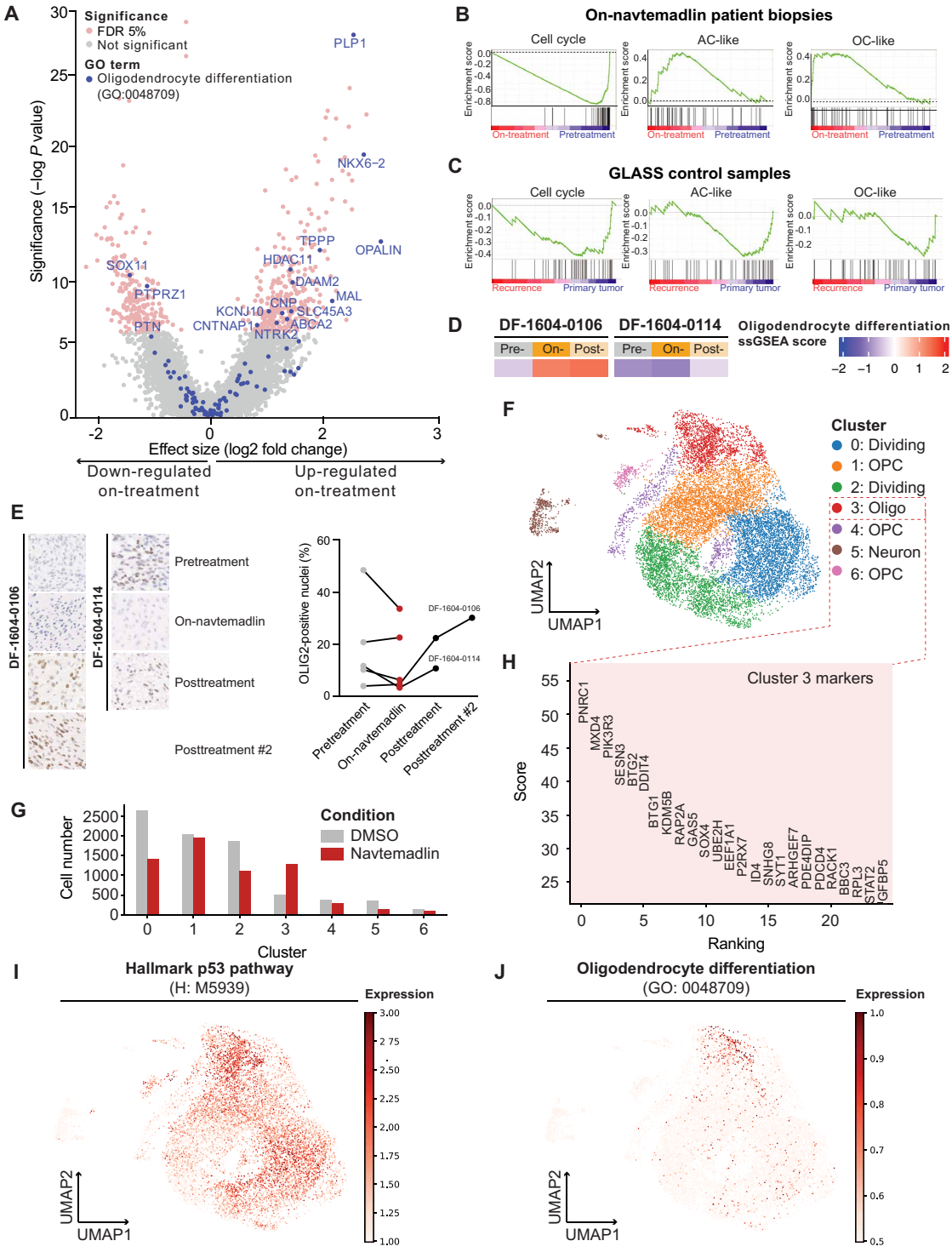

Fig. 5. Effect of navtemadlin in glioma cell differentiation. (**A**) Volcano plot showing differentially expressed genes on navtemadlin treatment (red; FDR cutoff 5%) compared with pretreatment samples. Blue circles indicate genes associated with oligodendrocyte differentiation (GO: 0048709). (**B** and **C**) GSEA in (B) on-navtemadlin patient biopsies and (C) GLASS control samples using the cell state signatures described in (27). (**D**) Oligodendrocyte differentiation ssGSEA scores for two patients with pretreatment, on-navtemadlin, and posttreatment samples. (**E**) Detection of OLIG2-positive tumor cells by immunohistochemistry (left) with quantification of OLIG2-positive nuclei in available pretreatment, on-navtemadlin, and posttreatment samples (right). (**F**) UMAP unsupervised clustering of BT145 cells treated with 50 nM navtemadlin or DMSO control. (**G**) Number of cells per condition present in each cluster. (**H**) Markers defining cluster 3 when compared with remaining clusters. (**I** and **J**) Expression of (I) hallmark p53 pathway and (J) oligodendrocyte differentiation gene signatures in BT145 cells and projection on the UMAP.

Alternative dosing schedules, such as single high-dose pulses, have been reported to increase apoptosis in *TP53* wild-type, *MDM2*-amplified osteosarcoma cells with a different MDM2 inhibitor (*21*). We did not observe increases in cell death rates at 6 days when pulsing navtemadlin for 12 hours in GBM cell lines, but our results suggested that higher concentrations of drug (>500 nM) may be required to achieve complete tumor cell killing. A second strategy is to test more potent MDM2 inhibitors with increased brain penetrance, such as the MDM2 inhibitor BI-907828 (*11*), which acts at a picomolar concentration in vitro and is currently being evaluated in patients with advanced or metastatic *TP53* wild-type solid tumors (NCT03449381). Thirdly, it will be critical to consider combination therapy with agents that exhibit nonoverlapping mechanisms of action with MDM2 inhibition. Here, we have shown the potential of combining navtemadlin with TMZ in *MGMT*-methylated tumors. One major concern is the potential induction of thrombocytopenia by both navtemadlin and TMZ; although in vivo testing of this drug combination remains to be conducted in mouse xenograft models, bone marrow cells were much more tolerant of the combination than glioma cells in vitro. In this regard, the bone marrow cell cultures recovered from cell cycle arrest and resumed proliferation after discontinuation of in vitro treatment, rather than showing commitment to apoptotic cell death. Moreover, myeloid suppression is a standard feature of widely used treatments for other cancers (*39*) and can be managed with a combination of cytokine-based myeloid stimulation and transfusions. The combination approach thus has the potential to extend the population of patients eligible for therapy with MDM2 inhibitors.

This study has provided evidence that navtemadlin's effectiveness may be enhanced with agents that increase replication stress. However, patients with unmethylated *MGMT* are unlikely to benefit from combinations that include navtemadlin with TMZ. Because radiotherapy also induces replication stress, the phase 1 component of this trial (NCT03107780) comprised a dose-escalation study combining navtemadlin with radiation in patients with newly diagnosed, *MGMT*-unmethylated, TP53 wild-type GBM within Alliance.

MATERIALS AND METHODS

Study design

The phase 0 surgical cohort of ABTC protocol 1604 (NCT03107780) enrolled adult participants with recurrent GBM who were planned for surgical resection. Additional eligibility criteria included Karnofsky Performance Status (KPS) $\geq$ 60% as well as normal organ and marrow function. Any number of prior therapies including prior bevacizumab use (after a washout of 6 weeks from bevacizumab) was allowed in the study. Use of enzyme-inducing antiepileptics, anticoagulants (other than low–molecular-weight heparin and prophylactic low-dose warfarin), and tumor-treating fields was not allowed in the study. Before surgery, participants were sequentially allocated to receive navtemadlin at either 120 mg daily or 240 mg daily for 2 days before surgery. Surgery was performed 3 to 6 hours after the last administration of navtemadlin. Blood samples for measurement of MIC-1 concentrations were collected at baseline/screening, on the day before surgery before the first dose, and 24 hours after the first dose but before the second dose on the day of surgery. Upon adequate recovery from surgery, participants whose tumors were *TP53* wild type were eligible to continue navtemadlin at the recommended phase 2 dose for monotherapy (240 mg daily for 7 days every 3 weeks) until progression or unacceptable toxicity. Eligibility for entry into the study was not restricted on the basis of *TP53* status, but *TP53* sequencing was performed on tumor tissues resected in the study, and only those patients with *TP53* wild-type tissues were meant to receive postoperative navtemadlin. This study was approved by the human investigations committee at each institution and registered on clinicaltrials.gov (NCT03107780). Written informed consent was obtained from each participant.

Pharmacokinetics

Navtemadlin concentrations in brain tissues were measured by a validated LC-MS/MS method over the range of 1 to 1000 ng/ml (*40*). Descriptive statistics were used to summarize the PK results of contrast- and non–contrast-enhancing brain tissues.

Evaluation of brain drug distribution by MALDI mass spectrometry imaging

Frozen tissue specimens were cryosectioned to a 10-μm thickness and thaw mounted onto indium tin oxide–coated glass slides. Consecutive sections were mounted onto microscopy slides, stained with H&E, and imaged with a 10× objective (Zeiss Observer Z.1). A matrix solution of 2,5-dihydroxybenzoic acid (160 mg/ml) in 70% methanol:30% trifluoroacetic acid and 1% dimethyl sulfoxide (DMSO) was applied to tissue sections using a robotic sprayer (HTX Technologies) using a two-pass cycle with a flow rate of 0.18 ml/min, a spray nozzle velocity of 1200 mm/min, a nitrogen gas pressure of 10 psi (68947.6 Pa), spray nozzle temperature of 75°C, and a track spacing of 2 mm. Recrystallization was performed using 5% acetic acid solution at 85°C for 6 min. Mass spectrometry imaging data were acquired using a timsTOF fleX mass spectrometer (Bruker Daltonics) in positive ion mode with a multiple reaction monitoring (MRM) method scanning across m/z (mass/charge ratio) 100 to 650. The mass spectrometry method was developed and optimized by direct infusion of a navtemadlin solution in the electrospray ionization source for a transition of the precursor ion from 568.168 to 301.051 (collision energy 45 eV, 3 m/z isolation window). Data were analyzed and visualized using SCiLS Lab software (version 2021a premium, Bruker Daltonics) with a total ion current (TIC) normalization.

Pharmacodynamics

For PD analysis from peripheral blood, a commercially available human GDF-15 Quantikine ELISA kit (R&D Systems) was used to measure serum MIC-1 concentrations over the range of 23.4 to 1500 pg/ml with dilutions up to 1:50 (v/v) being validated. Because serum MIC-1 changes in a concentration-time–like profile, samples lacking a paired predose baseline were not used in the analysis (*41*). This excluded six patients from the 120-mg cohort and four patients from the 240-mg cohort. The FCB analysis was performed on the predose samples that were obtained on the day of surgery. Two baseline measurements were obtained to assess the variability in the baseline to ensure robustness in the assessment of whether navtemadlin altered MIC-1 sufficiently. Descriptive statistics were used to summarize the results.

Immunohistochemistry

An expert neuropathologist (K.L.L.) reviewed histological patient tumor samples by WHO 2016 criteria, and the integrated diagnosis was confirmed by sequencing. Drug effects on tumor tissues were

evaluated on formalin-fixed paraffin sections using the Envision DAB staining system (DAKO). To assess drug modulation of the p53 pathway, the following antibodies were used: mouse monoclonal anti-p53 (Agilent, clone M7001, 1:100), mouse monoclonal anti-MDM2 (Millipore Sigma, clone OP46, 1:50), rabbit monoclonal anti-p21 (Cell Signaling Technology, clone 12D1, 1:50), rabbit polyclonal anti-phospho-CDK1 (Thermo Fisher Scientific, clone PA5-85508, 1:500), rabbit monoclonal anti-cleaved-caspase 3 (Cell Signaling Technology, clone 5A1E, 1:2000), and mouse monoclonal anti-Ki67 (Agilent, clone M7240, 1:100). Pathway response was assessed by quantification of the percentage of nuclei staining positively for each target using HALO AI digital pathology software (v3.6 Indica Labs) on whole-slide images. Artifact areas such as air bubbles or ink marks were manually excluded. The Nuclei Seg network detection algorithm was used to segment the boundaries of cell nuclei on the basis of staining intensity and morphology. A HALO Multiplex IHC v3.4 analyzer was used to identify positively stained nuclei according to specific staining intensity thresholds.

Tissue-based cyclic immunofluorescence

FFPE tumor blocks were sectioned into 5-μM sections and mounted on glass slides. A total of 36-plex immunofluorescent images were obtained from the sections using t-CyCIF imaging (*42*). The BOND RX Automated IHC/ISH Stainer was used to bake, dewax, and perform antigen retrieval (Leica Biosystems, Buffalo Grove, IL). Tissues underwent 12 cycles of antibody incubation, imaging, and fluorophore inactivation; a list of all antibodies used is provided in table S1. Images were obtained using the CyteFinder instrument (RareCyte) with a 20× objective lens. The resulting images were processed using the MCMICRO pipeline (*43*), which includes background subtraction, tile stitching, image registration, single-cell segmentation, and feature extraction. Data cleaning and quality control were subsequently performed using CyLinter software (*44*).

Nucleic acid extraction and bulk RNA-seq

For the analysis of human biopsies, FFPE tumor blocks were sectioned into 40-μM scrolls using a microtome. DNA and RNA were extracted simultaneously from each sample using the AllPrep DNA/RNA FFPE kit (80234, Qiagen). Before nucleic acid extraction, paraffin was dissolved using a deparaffinization solution (19093, Qiagen). To extract RNA from BT145 and BT286 cell lines, 2 million cells were collected after treatment with 50 nM navtemadlin for 30 hours. Next, RNA was isolated using the RNeasy Mini kit with an on-column DNase digestion (79254, Qiagen). Resulting RNA concentrations were quantified with a Nanodrop 2000 spectrophotometer (ND-2000, Thermo Scientific), and up to 500 ng was submitted for total RNA-seq on an Illumina NovaSeq instrument at the Molecular Biology Core Facilities of Dana-Farber Cancer Institute. Here, samples were subjected to rRNA depletion using the QIAseq FastSelect-rRNA HMR kit (334385, Qiagen), and sequencing was performed to generate 50 million 150–base pair read pairs (100 million reads) per sample. Quality control, alignment, and initial analyses were performed with VIPER (*45*). For both human tumor samples and cell lines, differentially expressed genes were calculated with the DESeq2 pipeline (*46*). For the analysis of GBMs treated with SOC, transcript counts and clinical data for the samples reported in (*47*) were downloaded from the GLASS consortium (https://glass-consortium.org). Significantly dysregulated genes were chosen on the basis of FDR $\leq$ 5% and $\log_2$ fold change $\pm$ 1 cutoffs.

Pathway analysis

Count matrices from sequenced tumors and cell lines were subject to GSEA using the GSEA 4.2.3 software implementation. To determine cellular effects associated with treatment, navtemadlin-treated samples and GLASS controls were analyzed using the hallmark gene sets from the Human MSigDB collection (*48*). Enrichment analysis for cell differentiation signatures was conducted using the cell cycle, astrocytic differentiation (AC-like), oligodendrocytic differentiation (OC-like), and oligodendrocyte precursor cell (OPC)–like programs described in (*27*). To assess p53 pathway activation in BT145 and BT286 patient-derived neurosphere models, we first identified differentially expressed genes in cells treated with 50 nM navtemadlin for 30 hours relative to DMSO control. We detected 390 and 132 dysregulated genes in BT145 and BT286 cells, respectively, with 125 genes (31 up-regulated and 94 down-regulated) being commonly dysregulated in both cell lines. We then used these 125 genes to construct custom gene sets of p53 pathway up-regulation and down-regulation. Last, we performed enrichment analysis of navtemadlin-treated human tumors and GLASS controls using these gene sets.

Single-cell RNA-seq and analysis

All single-cell data were analyzed in Python 3.9.7 using Scanpy 1.7.0, Matplotlib 3.6.2, and Pandas 1.4.3. Total RNA read counts were normalized to 10,000 to control for variability in sequencing depth between cells. The data were then log transformed and scaled to unit variance while clipping logread counts to 10 to reduce the effect of outliers. Unhealthy cells with a mitochondrial content greater than 20% were filtered out as well as cells expressing fewer than 200 genes. Last, we included only highly variable genes and genes belonging to our gene sets of interest in our analysis to reduce noise from housekeeping genes. Genes were deemed highly variable using the highly_variable_genes function in Scanpy with default settings, which uses a measure of the variance of a gene across cells relative to its average expression. All plots were generated using the Scanpy and Matplotlib libraries. To visualize the data, we reduced the data using principal components analysis, with the arpack singular-value decomposition solver, and used the top 40 principal components to produce a neighborhood graph with a hard cutoff at 10 neighbors using the pca and neighbors functions, respectively. This allowed us to embed the data into two dimensions into a UMAP plot using Scanpy's umap function. Pathway activation was scored on the basis of a cell's average expression of constituent genes in a pathway. Clustering was performed by Scanpy's leiden function (*29*), at a resolution of 0.2, which is a hierarchical algorithm that recursively merges communities of cells into progressively larger nodes.

Cell culture

The patient-derived neurosphere cell lines BT145, BT286, and BT359 were obtained from the Center for Patient-Derived Models at the Dana-Farber Cancer Institute. Human BMMCs immortalized with human telomerase reverse transcriptase were commercially acquired (T0523, Abm). Neurosphere models were grown in tumor stem medium (TSM), consisting of Neurobasal-A (10888022, Gibco), Dulbecco's modified Eagle's medium (DMEM)/F-12 (11330057, Gibco), sodium pyruvate (11360-070, Life Technologies), Hepes (15630-080, Life Technologies), Glutamax (35050-061, Life Technologies), nonessential amino acids (11140-050, Gibco), and 1% penicillin-streptomycin (15140-122, Life Technologies), and supplemented with B-27 (17504044, Gibco) and a growth factor mix consisting of 0.2% heparin (7980, STEMCELL

Technologies), basic fibroblast growth factor (20 g/ml; 78002.2, Stem Cell), and epidermal growth factor (20 g/ml; 78006.2, Stem Cell). BMMCs were grown adherently in plastic coated with Geltrex (A1413302, Fisher Scientific) and cultured in RPMI 1640 medium (11875093, Gibco) supplemented with 10% fetal bovine serum (FBS; Gemini Bio, catalog no. 100-800), 1% penicillin-streptomycin, and 10 M hydrocortisone (Sigma-Aldrich, catalog no. H0888-5G). Human embryonic kidney (HEK) 293T cells were grown in DMEM (12491, Gibco) supplemented with 10% FBS. All cell lines were maintained at 37°C in 5% CO_2, examined for mycoplasma contamination using the MycoAlert mycoplasma detection kit (LT07–518, Lonza), and subjected to short-tandem repeat (STR) profiling at the Molecular Diagnostics Laboratory of the Dana-Farber Cancer Institute.

Generation of MMR-deficient and TP53-null cells

To generate virus, Lipofectamine 3000 (L3000001, Thermo Fisher Scientific) reagents were used to transfect HEK293T cells with 10 μg of psPAX2 (12260, Addgene) and 1 μg of VSVG (12259, Addgene) viral packaging plasmids, as well as 10 μg of the pLX-311-Cas9 lentiviral vector (118018, Addgene) or the all-in-one pXPR_BRD051 vector containing guide RNAs targeting the *TP53* (GAAGGGACAGAAGATGACAG), *MSH2* (ATTCTGTTCTTATCCATGAG), or *MLH1* (GAGATGATTGAGAACTGGTA) genes (obtained from the Genetic Perturbation Platform at the Broad Institute of MIT and Harvard). Virus was harvested 48 hours later with the use of a 0.45-μm syringe filter. For transduction of the different lentiviral plasmids, BT145 cells were seeded at a density of 2 million cells per well in a 12-well plate (353225, Corning). Virus was added together with 5 μg ml^{-1} of polybrene, and cells were centrifuged at 2000 rpm for 2 hours at 30°C. BT145 cells were first transduced with the Cas9 plasmid and selected with blasticidin (10 μg/ml; A1113902, Gibco) for 7 days. To generate knockout cells, BT145 Cas9-expressing cells were transduced again with pXPR_BRD051 virus containing guide RNAs against the desired genes and selected with hygromycin (100 μg/ml; 10687010, Gibco) for 10 days.

Immunoblotting

Pellets from 3 million cells were lysed with radioimmunoprecipitation assay lysis buffer (9806S, Cell Signaling Technology) along with a protease and phosphatase inhibitor cocktail (PI-285, Boston BioProducts) and phenylmethylsulfonyl fluoride (8553S, Cell Signaling Technology). Lysates were incubated for 45 min on ice with pulse vortexing in 15-min intervals and centrifuged at 13,000 rpm for 10 min at 4°C. Protein concentrations were then quantified by the bicinchoninic acid (BCA) assay against a bovine serum albumin standard. Absorbance was measured by incubating protein samples and BCA standards with Pierce A/B colorimetric reagents (23227, Thermo Fisher Scientific). A total of 30 μg of protein was loaded for each sample in a NuPAGE 4 to 12% bis-tris gel (NP0335BOX, Invitrogen) and run with 1× NuPAGE MOPS running buffer (NP001, Life Technologies) for 1.5 hours at 120 V. For protein size comparison, the Cytiva full-range Rainbow molecular weight marker (RPN800E, Thermo Fisher Scientific) was used as a standard. After protein separation, a dry transfer was completed at 30 V for 6 min with polyvinylidene difluoride stacks in an iBlot 2 transfer instrument (IB24002, Invitrogen). After gel transfer, the membrane was blocked with 5% dry milk (1706404, Bio-Rad) in tris-buffered saline with Tween 20 (TBS-T; T1680, Thermo Fisher Scientific) for 30 min. Primary incubation with antibodies against rabbit p53 (2527S, Cell Signaling Technology), rabbit PUMA (12450S, Cell Signaling Technology), rabbit CDKN1A/p21 (2947S, Cell Signaling Technology), rabbit MDM2 (86934S, Cell Signaling Technology), and rabbit glyceraldehyde-3-phosphate dehydrogenase (GAPDH; 5174S, Cell Signaling Technology) at a 1:1000 dilution occurred overnight at 4°C. After washes with TBS-T, the membrane was incubated with an anti-rabbit secondary antibody (7074S, Cell Signaling Technology) at a 1:3000 dilution for 1 hour at room temperature. For the detection of apoptosis, a primary apoptosis antibody cocktail (Ab136812, Abcam) was used at a 1:250 dilution followed by a horseradish peroxidase cocktail at a 1:100 dilution. Signal was detected by chemiluminescence with Super-Signal West Pico (34095, Life Technologies) and Femto kits (34580, Life Technologies) in an ImageQuant LAS 4000 imager (GE Healthcare Life Sciences). When needed, membranes were stripped with Restore Plus Western blot stripping buffer (46430, Thermo Fisher Scientific) for 15 min, washed with TBS-T, and blocked with 5% milk and TBS-T for 30 min. Blots were quantified using ImageJ 1.52k software (NIH, USA), where band intensity was normalized against the loading control and expressed relative to the untreated condition.

Growth curves

Cell growth was tracked in real time using the IncuCyte S3 Live Cell Analysis System (Sartorius). Mesenchymal bone marrow cells, which grow adherently, were seeded at a density of 5000 per well in a clear 96-well plate (353075, Corning) precoated with 1× Geltrex (A1569601, Thermo Fisher Scientific). The next day, drug treatment was initiated and images were captured using a 10× objective every 6 hours. Cell confluency was determined for each condition in six technical replicates. For neurosphere cell lines (BT145, BT286, and BT359), cells were seeded in ultralow attachment round-bottom 96-well plates (7007, Corning) at a density of 500 cells per well. After a centrifugation for 15 min at 200*g*, the plates were inserted in the IncuCyte system, and images were acquired every 6 hours using the 4× objective. The neurosphere diameter was measured in ImageJ 1.52k (NIH, USA).

Dose-response curves and drug synergy analysis

Patient-derived neurosphere models (BT145, BT286, and BT359) and BMMCs were treated with the MDM2 inhibitor navtemadlin (HY-12296, MedChem Express) and TMZ (S1237, Selleckchem) as single agents or in combination. To assess growth relative to a DMSO (12611, Cell Signaling Technology) control, 5000 cells per well were seeded in triplicate in a 96-well white bottom plate (136102, Thermo Fisher Scientific). Drug treatments with navtemadlin as monotherapy lasted >72 hours, whereas experiments involving TMZ were extended to >120 hours to allow for bioactivation of this prodrug. The CellTiter-Glo assay (G9681, Promega) was used to measure amounts of ATP as a surrogate for cell viability. Briefly, the reagent mixture was added in a 1:1 ratio to the 96-well plate, which was then incubated at room temperature for 15 min. Luminescence measurements were acquired in a SpectraMax M5 plate reader (Associated Technologies Group) with an integration time of 500 ms. The data were analyzed in GraphPad Prism. Potential synergy between navtemadlin and TMZ was calculated using the web 3.0 version of SynergyFinder, where multidose viability data were uploaded for each cell line. The degree of combination synergy was quantified by the HSA model.

Detection of apoptosis by flow cytometry

Cell death fractions after treatment with navtemadlin and/or TMZ were detected with an Alexa Fluor 488 annexin V/Dead Cell Apoptosis

kit (V13241, Thermo Fisher Scientific). For bone marrow cells, which are green fluorescent protein (GFP) positive, an Alexa Fluor 647 annexin V antibody (A23204, Thermo Fisher Scientific) was used instead. Briefly, 1 million cells were pelleted and resuspended in 1× annexin-binding buffer (50 mM Hepes, 700 mM NaCl, and 12.5 mM $CaCl_2$) containing 1:20 annexin V antibody and PI (1 μg/ml). After a 15-min incubation at room temperature, cells were analyzed in a Fortessa 3 flow analyzer (BD Biosciences). Here, single cells were first gated using forward scatter and side scatter parameters and were later classified into four quadrants on the basis of whether they were negative for both stains (viable), annexin V positive (early apoptotic), PI positive (necrotic), or positive for both stains (late apoptotic). The fraction of apoptotic cells was then calculated by adding the percentage of cells in the early and late apoptotic quadrants. Samples were measured in triplicate and analyzed in FlowJo 10.8.1.

Statistical analysis

Analyses of bulk and single-cell RNA-seq data were performed as described in the Materials and Methods subsections above, with significance cutoffs of FDR ≤ 5% for differential gene expression analysis. Synergy analysis was performed as described in the Materials and Methods subsection "Dose-response curves and drug synergy analysis." Statistical analyses for immunohistochemistry, immunofluorescence, gene expression, BH3 mimetics, and flow cytometry experiments were conducted in GraphPad Prism 10. Comparisons between two groups (for example, gene expression before and after navtemadlin treatment) were done using Wilcoxon rank sum tests. When performing comparisons across multiple groups (for example, apoptotic rates between navtemadlin-treated, TMZ-treated, or combination-treated cells), *P* values were corrected for multiple hypotheses using a Bonferroni correction. When comparing the effect of more than two conditions (for example, how cells grow after treatment with different drugs and knocking out different genes), we used a two-way analysis of variance (ANOVA) followed by Dunnett's post hoc tests. Statistical tests for each experiment are described in each figure legend. Cell numbers, seeding densities, and replicates are provided in the figure legends as well. All bar charts indicate the mean ± SD, whereas growth curves in Figs. 4D and 5A and fig. S7D indicate the mean ± SE.

Supplementary Materials

The PDF file includes:
Figs. S1 to S7
Table S1

Other Supplementary Material for this manuscript includes the following:
Data file S1
MDAR Reproducibility Checklist

REFERENCES AND NOTES

1. Y. Zhang, C. Dube, M. Gibert Jr., N. Cruickshanks, B. Wang, M. Coughlan, Y. Yang, I. Setiady, C. Deveau, K. Saoud, C. Grello, M. Oxford, F. Yuan, R. Abounader, The p53 pathway in glioblastoma. *Cancer* **10**, 297 (2018).
2. M. Fischer, Census and evaluation of p53 target genes. *Oncogene* **36**, 3943–3956 (2017).
3. L. T. Vassilev, Small-molecule antagonists of p53-MDM2 binding: Research tools and potential therapeutics. *Cell Cycle* **3**, 419–421 (2004).
4. L. T. Vassilev, B. T. Vu, B. Graves, D. Carvajal, F. Podlaski, Z. Filipovic, N. Kong, U. Kammlott, C. Lukacs, C. Klein, N. Fotouhi, E. A. Liu, In vivo activation of the p53 pathway by small-molecule antagonists of MDM2. *Science* **303**, 844–848 (2004).
5. Y. Rew, D. Sun, Discovery of a small molecule MDM2 inhibitor (AMG 232) for treating cancer. *J. Med. Chem.* **57**, 6332–6341 (2014).
6. W. L. Gluck, M. M. Gounder, R. Frank, F. Eskens, J. Y. Blay, P. A. Cassier, J.-C. Soria, S. Chawla, V. de Weger, A. J. Wagner, D. Siegel, F. De Vos, E. Rasmussen, H. A. Henary, Phase 1 study of the MDM2 inhibitor AMG 232 in patients with advanced P53 wild-type solid tumors or multiple myeloma. *Invest. New Drugs* **38**, 831–843 (2020).
7. M. M. Gounder, T. M. Bauer, G. K. Schwartz, P. LoRusso, P. Kumar, K. Kato, B. Tao, Y. Hong, P. Patel, D. Hong, Milademetan, an oral MDM2 inhibitor, in well-differentiated/dedifferentiated liposarcoma: Results from a phase 1 study in patients with solid tumors or lymphomas. *Eur. J. Cancer* **138**, S3–S4 (2020).
8. A. Mullard, p53 programmes plough on. *Nat. Rev. Drug Discov.* **19**, 497–500 (2020).
9. M. Verreault, C. Schmitt, L. Goldwirt, K. Pelton, S. Haidar, C. Levasseur, J. Guehennec, D. Knoff, M. Labussière, Y. Marie, A. H. Ligon, K. Mokhtari, K. Hoang-Xuan, M. Sanson, B. M. Alexander, P. Y. Wen, J.-Y. Delattre, K. L. Ligon, A. Idbaih, Preclinical efficacy of the MDM2 inhibitor RG7112 in MDM2-amplified and TP53 wild-type glioblastomas. *Clin. Cancer Res.* **22**, 1185–1196 (2016).
10. N.-G. Her, J.-W. Oh, Y. J. Oh, S. Han, H. J. Cho, Y. Lee, G. H. Ryu, D.-H. Nam, Potent effect of the MDM2 inhibitor AMG232 on suppression of glioblastoma stem cells. *Cell Death Dis.* **9**, 792 (2018).
11. X. Hao, R. Bahia, O. Cseh, D. Bozek, S. Blake, J. Rinnenthal, U. Weyer-Czernilofsky, D. Rudolph, H. A. Luchman, BI-907828, a novel potent MDM2 inhibitor, inhibits GBM brain tumor stem cells in vitro and prolongs survival in orthotopic xenograft mouse models. *Neuro Oncol.* **25**, 913–926 (2023).
12. H. Zhu, H. Gao, Y. Ji, Q. Zhou, Z. Du, L. Tian, Y. Jiang, K. Yao, Z. Zhou, Targeting p53-MDM2 interaction by small-molecule inhibitors: Learning from MDM2 inhibitors in clinical trials. *J. Hematol. Oncol.* **15**, 91 (2022).
13. S. A. Grossman, C. G. Romo, M. A. Rudek, J. Supko, J. Fisher, L. B. Nabors, P. Y. Wen, D. M. Peereboom, B. M. Ellingson, W. Elmquist, F. G. Barker, D. Kamson, J. N. Sarkaria, W. Timmer, R. S. Bindra, X. Ye, Baseline requirements for novel agents being considered for phase II/III brain cancer efficacy trials: Conclusions from the Adult Brain Tumor Consortium's first workshop on CNS drug delivery. *Neuro Oncol.* **22**, 1422–1424 (2020).
14. H. Yang, Z. Filipovic, D. Brown, S. N. Breit, L. T. Vassilev, Macrophage inhibitory cytokine-1: A novel biomarker for p53 pathway activation. *Mol. Cancer Ther.* **2**, 1023–1029 (2003).
15. H. P. Erba, P. S. Becker, P. J. Shami, M. R. Grunwald, D. L. Flesher, M. Zhu, E. Rasmussen, H. A. Henary, A. A. Anderson, E. S. Wang, Phase 1b study of the MDM2 inhibitor AMG 232 with or without trametinib in relapsed/refractory acute myeloid leukemia. *Blood Adv.* **3**, 1939–1949 (2019).
16. A. Subramanian, P. Tamayo, V. K. Mootha, S. Mukherjee, B. L. Ebert, M. A. Gillette, A. Paulovich, S. L. Pomeroy, T. R. Golub, E. S. Lander, J. P. Mesirov, Gene set enrichment analysis: A knowledge-based approach for interpreting genome-wide expression profiles. *Proc. Natl. Acad. Sci. U.S.A.* **102**, 15545–15550 (2005).
17. L. Haronikova, O. Bonczek, P. Zatloukalova, F. Kokas-Zavadil, M. Kucerikova, P. J. Coates, R. Fahraeus, B. Vojtesek, Resistance mechanisms to inhibitors of p53-MDM2 interactions in cancer therapy: Can we overcome them? *Cell. Mol. Biol. Lett.* **26**, 53 (2021).
18. I. Ray-Coquard, J.-Y. Blay, A. Italiano, A. Le Cesne, N. Penel, J. Zhi, F. Heil, R. Rueger, B. Graves, M. Ding, D. Geho, S. A. Middleton, L. T. Vassilev, G. L. Nichols, B. N. Bui, Effect of the MDM2 antagonist RG7112 on the P53 pathway in patients with MDM2-amplified, well-differentiated or dedifferentiated liposarcoma: An exploratory proof-of-mechanism study. *Lancet Oncol.* **13**, 1133–1140 (2012).
19. M. Andreeff, K. R. Kelly, K. Yee, S. Assouline, R. Strair, L. Popplewell, D. Bowen, G. Martinelli, M. W. Drummond, P. Vyas, M. Kirschbaum, S. P. Iyer, V. Ruvolo, G. M. N. González, X. Huang, G. Chen, B. Graves, S. Blotner, P. Bridge, L. Jukofsky, S. Middleton, M. Reckner, R. Rueger, J. Zhi, G. Nichols, K. Kojima, Results of the phase I trial of RG7112, a small-molecule MDM2 antagonist in leukemia. *Clin. Cancer Res.* **22**, 868–876 (2016).
20. J. Canon, T. Osgood, S. H. Olson, A. Y. Saiki, R. Robertson, D. Yu, J. Eksterowicz, Q. Ye, L. Jin, A. Chen, J. Zhou, D. Cordover, S. Kaufman, R. Kendall, J. D. Oliner, A. Coxon, R. Radinsky, The MDM2 inhibitor AMG 232 demonstrates robust antitumor efficacy and potentiates the activity of p53-inducing cytotoxic agents. *Mol. Cancer Ther.* **14**, 649–658 (2015).
21. S. Jeay, S. Ferretti, P. Holzer, J. Fuchs, E. A. Chapeau, M. Wartmann, D. Sterker, V. Romanet, M. Murakami, G. Kerr, E. Y. Durand, S. Gaulis, M. Cortes-Cros, S. Ruetz, T.-M. Stachyra, J. Kallen, P. Furet, J. Würthner, N. Guerreiro, E. Halilovic, A. Jullion, A. Kauffmann, E. Kuriakose, M. Wiesmann, M. R. Jensen, F. Hofmann, W. R. Sellers, Dose and schedule determine distinct molecular mechanisms underlying the efficacy of the p53-MDM2 inhibitor HDM201. *Cancer Res.* **78**, 6257–6267 (2018).
22. D. S. Potter, A. Letai, To prime, or not to prime: That is the question. *Cold Spring Harb. Symp. Quant. Biol.* **81**, 131–140 (2016).
23. I. M. Forte, P. Indovina, C. A. Iannuzzi, D. Cirillo, D. Di Marzo, D. Barone, F. Capone, F. Pentimalli, A. Giordano, Targeted therapy based on p53 reactivation reduces both glioblastoma cell growth and resistance to temozolomide. *Int. J. Oncol.* **54**, 2189–2199 (2019).
24. S. R. Punganuru, V. Artula, W. Zhao, M. Rajaei, H. Deokar, R. Zhang, J. K. Buolamwini, K. S. Srivenugopal, W. Wang, Targeted brain tumor therapy by inhibiting the MDM2 oncogene: In vitro and in vivo antitumor activity and mechanism of action. *Cells* **9**, 1592 (2020).
25. M. Touat, Y. Y. Li, A. N. Boynton, L. F. Spurr, J. B. Iorgulescu, C. L. Bohrson, I. Cortes-Ciriano, C. Birzu, J. E. Geduldig, K. Pelton, M. J. Lim-Fat, S. Pal, R. Ferrer-Luna, S. H. Ramkissoon,

F. Dubois, C. Bellamy, N. Currimjee, J. Bonardi, K. Qian, P. Ho, S. Malinowski, L. Taquet, R. E. Jones, A. Shetty, K.-H. Chow, R. Sharaf, D. Pavlick, L. A. Albacker, N. Younan, C. Baldini, M. Verreault, M. Giry, E. Guillerm, S. Ammari, F. Beuvon, K. Mokhtari, A. Alentorn, C. Dehais, C. Houillier, F. Laigle-Donadey, D. Psimaras, E. Q. Lee, L. Nayak, J. R. McFaline-Figueroa, A. Carpentier, P. Cornu, L. Capelle, B. Mathon, J. S. Barnholtz-Sloan, A. Chakravarti, W. L. Bi, E. A. Chiocca, K. P. Fehnel, S. Alexandrescu, S. N. Chi, D. Haas-Kogan, T. T. Batchelor, G. M. Frampton, B. M. Alexander, R. Y. Huang, A. H. Ligon, F. Coulet, J.-Y. Delattre, K. Hoang-Xuan, D. M. Meredith, S. Santagata, A. Duval, M. Sanson, A. D. Cherniack, P. Y. Wen, D. A. Reardon, A. Marabelle, P. J. Park, A. Idbaih, R. Beroukhim, P. Bandopadhayay, F. Bielle, K. L. Ligon, Mechanisms and therapeutic implications of hypermutation in gliomas. *Nature* **580**, 517–523 (2020).

26. S. Mehta, E. Huillard, S. Kesari, C. L. Maire, D. Golebiowski, E. P. Harrington, J. A. Alberta, M. F. Kane, M. Theisen, K. L. Ligon, D. H. Rowitch, C. D. Stiles, The central nervous system-restricted transcription factor Olig2 opposes p53 responses to genotoxic damage in neural progenitors and malignant glioma. *Cancer Cell* **19**, 359–371 (2011).
27. M. G. Filbin, I. Tirosh, V. Hovestadt, M. L. Shaw, L. E. Escalante, N. D. Mathewson, C. Neftel, N. Frank, K. Pelton, C. M. Hebert, C. Haberler, K. Yizhak, J. Gojo, K. Egervari, C. Mount, P. van Galen, D. M. Bonal, Q.-D. Nguyen, A. Beck, C. Sinai, T. Czech, C. Dorfer, L. Goumnerova, C. Lavarino, A. M. Carcaboso, J. Mora, R. Mylvaganam, C. C. Luo, A. Peyrl, M. Popović, A. Azizi, T. T. Batchelor, M. P. Frosch, M. Martinez-Lage, M. W. Kieran, P. Bandopadhayay, R. Beroukhim, G. Fritsch, G. Getz, O. Rozenblatt-Rosen, K. W. Wucherpfennig, D. N. Louis, M. Monje, I. Slavc, K. L. Ligon, T. R. Golub, A. Regev, B. E. Bernstein, M. L. Suvà, Developmental and oncogenic programs in H3K27M gliomas dissected by single-cell RNA-seq. *Science* **360**, 331–335 (2018).
28. K. L. Ligon, E. Huillard, S. Mehta, S. Kesari, H. Liu, J. A. Alberta, R. M. Bachoo, M. Kane, D. N. Louis, R. A. Depinho, D. J. Anderson, C. D. Stiles, D. H. Rowitch, Olig2-regulated lineage-restricted pathway controls replication competence in neural stem cells and malignant glioma. *Neuron* **53**, 503–517 (2007).
29. V. A. Traag, L. Waltman, N. J. van Eck, From Louvain to Leiden: Guaranteeing well-connected communities. *Sci. Rep.* **9**, 5233 (2019).
30. C. Birzu, P. French, M. Caccese, G. Cerretti, A. Idbaih, V. Zagonel, G. Lombardi, Recurrent glioblastoma: From molecular landscape to new treatment perspectives. *Cancer* **13**, 47 (2021).
31. K. Singh, K. M. Hotchkiss, I. F. Parney, J. De Groot, S. Sahebjam, N. Sanai, M. Platten, E. Galanis, M. Lim, P. Y. Wen, G. Minniti, H. Colman, T. F. Cloughesy, M. P. Mehta, M. Geurts, I. Arrillaga-Romany, A. Desjardins, K. Tanner, S. Short, D. Arons, E. Duke, W. Wick, S. J. Bagley, D. M. Ashley, P. Kumthekar, R. Verhaak, A. J. Chalmers, A. P. Patel, C. Watts, P. E. Fecci, T. T. Batchelor, M. Weller, M. A. Vogelbaum, M. Preusser, M. S. Berger, M. Khasraw, Correcting the drug development paradigm for glioblastoma requires serial tissue sampling. *Nat. Med.* **29**, 2402–2405 (2023).
32. C. Neftel, J. Laffy, M. G. Filbin, T. Hara, M. E. Shore, G. J. Rahme, A. R. Richman, D. Silverbush, M. L. Shaw, C. M. Hebert, J. Dewitt, S. Gritsch, E. M. Perez, L. N. Gonzalez Castro, X. Lan, N. Druck, C. Rodman, D. Dionne, A. Kaplan, M. S. Bertalan, J. Small, K. Pelton, S. Becker, D. Bonal, Q.-D. Nguyen, R. L. Servis, J. M. Fung, R. Mylvaganam, L. Mayr, J. Gojo, C. Haberler, R. Geyeregger, T. Czech, I. Slavc, B. V. Nahed, W. T. Curry, B. S. Carter, H. Wakimoto, P. K. Brastianos, T. T. Batchelor, A. Stemmer-Rachamimov, M. Martinez-Lage, M. P. Frosch, I. Stamenkovic, N. Riggi, E. Rheinbay, M. Monje, O. Rozenblatt-Rosen, D. P. Cahill, A. P. Patel, T. Hunter, I. M. Verma, K. L. Ligon, D. N. Louis, A. Regev, B. E. Bernstein, I. Tirosh, M. L. Suvà, An integrative model of cellular states, plasticity, and genetics for glioblastoma. *Cell* **178**, 835–849.e21 (2019).
33. I. Liu, L. Jiang, E. R. Samuelsson, S. Marco Salas, A. Beck, O. A. Hack, D. Jeong, M. L. Shaw, B. Englinger, J. LaBelle, H. M. Mire, S. Madlener, L. Mayr, M. A. Quezada, M. Trissal, E. Panditharatna, K. J. Ernst, J. Vogelzang, T. A. Gatesman, M. E. Halbert, H. Palova, P. Pokorna, J. Sterba, O. Slaby, R. Geyeregger, A. Diaz, I. J. Findlay, M. D. Dun, A. Resnick, M. L. Suvà, D. T. W. Jones, S. Agnihotri, J. Svedlund, C. Koschmann, C. Haberler, T. Czech, I. Slavc, J. A. Cotter, K. L. Ligon, S. Alexandrescu, W. K. A. Yung, I. Arrillaga-Romany, J. Gojo, M. Monje, M. Nilsson, M. G. Filbin, The landscape of tumor cell states and spatial organization in H3-K27M mutant diffuse midline glioma across age and location. *Nat. Genet.* **54**, 1881–1894 (2022).
34. Y. Hoogstrate, K. Draaisma, S. A. Ghisai, L. van Hijfte, N. Barin, I. de Heer, W. Coppieters, T. P. P. van den Bosch, A. Bolleboom, Z. Gao, A. J. P. E. Vincent, L. Karim, M. Deckers, M. J. B. Taphoorn, M. Kerkhof, A. Weyerbrock, M. Sanson, A. Hoeben, S. Lukacova, G. Lombardi, S. Leenstra, M. Hanse, R. E. M. Fleischeuer, C. Watts, N. Angelopoulos, T. Gorlia, V. Golfinopoulos, V. Bours, M. J. van den Bent, P. A. Robe, P. J. French, Transcriptome analysis reveals tumor microenvironment changes in glioblastoma. *Cancer Cell* **41**, 678–692.e7 (2023).
35. S. Bao, Q. Wu, R. E. McLendon, Y. Hao, Q. Shi, A. B. Hjelmeland, M. W. Dewhirst, D. D. Bigner, J. N. Rich, Glioma stem cells promote radioresistance by preferential activation of the DNA damage response. *Nature* **444**, 756–760 (2006).
36. J. Chen, Y. Li, T.-S. Yu, R. M. McKay, D. K. Burns, S. G. Kernie, L. F. Parada, A restricted cell population propagates glioblastoma growth after chemotherapy. *Nature* **488**, 522–526 (2012).
37. K. Palanichamy, J. R. Jacob, K. T. Litzenberg, A. Ray-Chaudhury, A. Chakravarti, Cells isolated from residual intracranial tumors after treatment express iPSC genes and possess neural lineage differentiation plasticity. *EBioMedicine* **36**, 281–292 (2018).
38. Z. Wang, H. Zhang, S. Xu, Z. Liu, Q. Cheng, The adaptive transition of glioblastoma stem cells and its implications on treatments. *Signal Transduct. Target. Ther.* **6**, 124 (2021).
39. D. J. Kuter, in *Consultative Hemostasis and Thrombosis,* C. S. Kitchens, C. M. Kessler, B. A. Konkle, M. B. Streiff, D. A. Garcia, Eds. (Elsevier, ed. 4, 2019), pp. 108–126.
40. A. B. Kagan, N. M. Anders, A. Hemingway, E. Q. Lee, K. R. Kelly, H. C. Lee, M. Xu-Welliver, R. Piekarz, M. A. Rudek, Quantitation of navtemadlin in human plasma and brain tissue by liquid chromatography-tandem mass spectrometry. *Biomed. Chromatogr.* **36**, e5467 (2022).
41. S. Wong, C. Krejsa, D. Lee, A. Harris, E. Simard, X. Wang, M. Allard, T. Podoll, T. O'Reilly, J. G. Slatter, Pharmacokinetics and macrophage inhibitory cytokine-1 pharmacodynamics of the murine double minute 2 inhibitor, navtemadlin (KRT-232) in fed and fasted healthy subjects. *Clin. Pharmacol. Drug Dev.* **11**, 640–653 (2022).
42. J.-R. Lin, B. Izar, S. Wang, C. Yapp, S. Mei, P. M. Shah, S. Santagata, P. K. Sorger, Highly multiplexed immunofluorescence imaging of human tissues and tumors using t-CyCIF and conventional optical microscopes. *eLife* **7**, e31657 (2018).
43. D. Schapiro, A. Sokolov, C. Yapp, Y.-A. Chen, J. L. Muhlich, J. Hess, A. L. Creason, A. J. Nirmal, G. J. Baker, M. K. Nariya, J.-R. Lin, Z. Maliga, C. A. Jacobson, M. W. Hodgman, J. Ruokonen, S. L. Farhi, D. Abbondanza, E. T. McKinley, D. Persson, C. Betts, S. Sivagnanam, A. Regev, J. Goecks, R. J. Coffey, L. M. Coussens, S. Santagata, P. K. Sorger, MCMICRO: A scalable, modular image-processing pipeline for multiplexed tissue imaging. *Nat. Methods* **19**, 311–315 (2022).
44. G. J. Baker, E. Novikov, Z. Zhao, T. Vallius, J. A. Davis, J.-R. Lin, J. L. Muhlich, E. A. Mittendorf, S. Santagata, J. L. Guerriero, P. K. Sorger, Quality control for single cell analysis of high-plex tissue profiles using CyLinter. bioRxiv 565120 [Preprint] (2024). https://doi.org/10.1101/2023.11.01.565120.
45. M. Cornwell, M. Vangala, L. Taing, Z. Herbert, J. Köster, B. Li, H. Sun, T. Li, J. Zhang, X. Qiu, M. Pun, R. Jeselsohn, M. Brown, X. S. Liu, H. W. Long, VIPER: Visualization pipeline for RNA-seq, a Snakemake workflow for efficient and complete RNA-seq analysis. *BMC Bioinform.* **19**, 135 (2018).
46. M. I. Love, W. Huber, S. Anders, Moderated estimation of fold change and dispersion for RNA-seq data with DESeq2. *Genome Biol.* **15**, 550 (2014).
47. Q. Wang, B. Hu, X. Hu, H. Kim, M. Squatrito, L. Scarpace, A. C. deCarvalho, S. Lyu, P. Li, Y. Li, F. Barthel, H. J. Cho, Y.-H. Lin, N. Satani, E. Martinez-Ledesma, S. Zheng, E. Chang, C.-E. G. Sauvé, A. Olar, Z. D. Lan, G. Finocchiaro, J. J. Phillips, M. S. Berger, K. R. Gabrusiewicz, G. Wang, E. Eskilsson, J. Hu, T. Mikkelsen, R. A. DePinho, F. Muller, A. B. Heimberger, E. P. Sulman, D.-H. Nam, R. G. W. Verhaak, Tumor evolution of glioma-intrinsic gene expression subtypes associates with immunological changes in the microenvironment. *Cancer Cell* **32**, 42–56.e6 (2017).
48. A. Liberzon, C. Birger, H. Thorvaldsdóttir, M. Ghandi, J. P. Mesirov, P. Tamayo, The Molecular Signatures Database (MSigDB) hallmark gene set collection. *Cell. Syst.* **1**, 417–425 (2015).

Acknowledgments: We thank the patients and their families for participating in the study. **Funding:** This study was sponsored by the Adult Brain Tumor Consortium (ABTC) NIH/NCI UM1 CA137443; NIH grants U54-CA210180 (N.Y.R.A.), P41-EB028741 (N.Y.R.A.), U19CA264504, R01CA262462 (R.B. and K.L.L.), and R01CA188228 (R.B. and K.L.L.); and a Capital Award from the Massachusetts Life Sciences Center. The project described was also supported by the Analytical Pharmacology Core of the Sidney Kimmel Comprehensive Cancer Center at Johns Hopkins (NIH grants P30CA006973 and UL1TR003098 and the Shared Instrument Grant S10RR026824), the Gray Matters Brain Cancer Research Foundation, Ludwig Center at Harvard (P.K.S. and S.S.), the 3000 Miles to the Cure Foundation (K.L.L.), the Brain Tumour Charity (V.R.), the Swedish Research Council (2022-01539; V.R.), the Swedish Cancer Society (23 0622 JIA; V.R.), the Berth van Kantzows Foundation (V.R.), and the National Library of Medicine (5T15LM007059-38; R.R.). The grant number UL1TR003098 is from the National Center for Advancing Translational Sciences (NCATS), a component of the National Institutes of Health (NIH), and the NIH Roadmap for Medical Research. Its contents are solely the responsibility of the authors and do not necessarily represent the official view of the NCATS or NIH. **Author contributions:** Conceptualization: V.R., E.Q.L., P.Y.W., K.L.L., and R.B. Methodology: V.R., E.Q.L., C.B., N.K., M.A.R., S.P., N.A., M.C., R.R., J.-R.L., A.R.N.R., A.C.R.F., G.A., S.M., J.J., S.A.S., J.S., and K. Pelton. Formal analysis: V.R., E.Q.L., C.B., N.K., M.S.R., S.P., N.A., M.C., R.R., J.-R.L., M.C., A.R.N.R., A.C.R.F., G.A., S.M., J.J., S.A.S., J.S., and X.Y. Investigation: V.R., E.Q.L., C.B., N.K., M.S.R., S.P., N.A., R.R., J.-R.L., M.C., A.R.N.R., A.C.R.F., G.A., S.M., J.J., S.A.S., and J.S. Resources: E.Q.L., M.S.R., A.D., F.L., K. Palanichamy, J.D.F., K. Pelton, R.Y.H., K.A.S., L.B.N., M.H., N.D., R.S., S.D., T.W., A.C., P.K.S., S.S., N.Y.R.A., S.A.G., B.M.A., P.Y.W., K.L.L., and R.B. Data curation: C.B., E.L., and W.P. Writing: V.R., E.Q.L., C.B., M.S.R., S.P., G.A., S.M., J.J., R.R., P.Y.W., K.L.L., and R.B. Visualization: V.R., E.Q.L., C.B., K.L.L., and R.B. Supervision: V.R., E.Q.L., P.Y.W., K.L.L., and R.B. Funding acquisition: V.R., E.Q.L., P.Y.W., K.L.L., and R.B. **Competing interests:** N.Y.R.A. is key opinion leader for Bruker Daltonics and receives support from Thermo Finnegan and EMD Serono. N.A. declares paid consulting for the National Brain Tumor Society. K.L.L. receives consulting fees from Travera, Servier, BMS, LEK, and Blaze Bioscience, as well as research funding to institution from BMS and Lily. R.B. receives

grant funding to institution from Novartis and Merck and consulting fees/equity from Scorpion Therapeutics and Karyoverse Therapeutics. The S.S. laboratory receives research funding from Merck. B.M.A. is also affiliated with Valo Health Partner (CEO), Flagship Pioneering (SVP R&D), Genentech (CEO), and Foundation Medicine. J.J. is also affiliated with Tufts University. All other authors declare that they have no competing interests. **Data and materials availability:** All data associated with this study are present in the paper or the Supplementary Materials. Patient-derived cell lines are available from K.L.L. under a material transfer agreement with the Dana-Farber Cancer Institute Center for Patient Derived Models. The survival and safety data from the clinical trial data are available through a data sharing agreement with the Dana-Farber Cancer Institute upon request to E.Q.L. Raw and processed RNA-seq data from neurospheres and human tumors have been deposited at Gene Expression Omnibus (GEO) under accession numbers GSE280891 and GSE280951, respectively.

Submitted 20 December 2023
Resubmitted 16 September 2024
Accepted 29 January 2025
Published 19 February 2025
10.1126/scitranslmed.adn6274